Carnegie Mellon University

CARNEGIE INSTITUTE OF TECHNOLOGY

THESIS

SUBMITTED IN PARTIAL FULFILLMENT OF THE REQUIREMENTS
FOR THE DEGREE OF

Doctor of Philosophy

TITLE Improving the Accuracy of Fluid-Structure Interaction Analyses of Patient-Specific Cerebral Aneurysms

PRESENTED BY Erick L. Johnson

ACCEPTED BY THE DEPARTMENT OF

Mechanical Engineering

Kenji Shimada — ADVISOR, MAJOR PROFESSOR — 8/2/2010 — DATE

ADVISOR, MAJOR PROFESSOR — 8/3/2010 — DATE

Nadine Aubry — DEPARTMENT HEAD — 8/9/2010 — DATE

APPROVED BY THE COLLEGE COUNCIL

Vijayakumar Bhagavatula — DEAN — 08/14/10 — DATE

IMPROVING THE ACCURACY OF FLUID-STRUCTURE INTERACTION ANALYSES OF PATIENT-SPECIFIC CEREBRAL ANEURYSMS

SUBMITTED IN PARTIAL FULFILLMENT OF THE REQUIREMENTS
FOR THE DEGREE OF
DOCTOR OF PHILOSOPHY
IN
DEPARTMENT OF MECHANICAL ENGINEERING,
CARNEGIE MELLON UNIVERSITY

Erick L. Johnson
B.S., Mechanical Engineering, Carnegie Mellon University

Carnegie Mellon University
Pittsburgh, PA
July, 2010

Keywords: Aneurysm, surface parameterization, mass-spring model, spring deformation, geometric modeling, boundary-layer meshing

Abstract

Accurate computational simulations are crucial to understanding the causes and potential treatment of the 27,000 cerebral aneurysms that rupture annually in the United States. While the accuracy and number of computational simulations has increased, modeling and meshing the geometry, and providing proper boundary and loading conditions remains a complex process. It is because of these complexities that most simulations rely on a uniform wall thickness with constant, isotropic material properties. Unfortunately, the stresses calculated for a cerebral aneurysm are highly susceptible to the quality of the model being used. This thesis addresses the issue of model fidelity and mesh quality by presenting algorithms to determine an approximate, or *equivalent*, wall thickness for patient-specific cerebral aneurysms and to create a new boundary-layer mesh sizing-function. The equivalent wall thickness is found by deforming the mesh of a healthy blood-vessel onto the aneurysm model, where the stretching of the mesh elements represents the weakening blood-vessel wall. A medial-ball based sizing function prevents overlapping in boundary-layer meshes and increases the usability of anisotropic, prismatic elements. With a more exact model of the aneurysm wall, clinicians will be provided multiphasic diagnostic, preventative, and curative information. Furthermore, future simulations will allow for early diagnosis and quantification of potential treatment options; with early intervention culminating in the best course of action being chosen for each individual patient. The contributions of this thesis are demonstrated through a series of fluid-structure interaction simulations, where use of the equivalent wall-thickness is shown to have a significant effect on the wall stresses. Furthermore, the deformation process used to calculate the equivalent wall thickness is shown to be able to map the anisotropic material directions of the vessel tissue onto the aneurysm itself.

Acknowledgements

I want to thank the unwavering support of my advisors Dr. Kenji Shimada (Committee Chair) and Dr. Yongjie Zhang, without whom I wouldn't have been pushed to my limits and survived. With them I've been able to perform incredible research, from scratch, that I wouldn't have dreamed of doing when I was looking for graduate schools. They have also provided the majority of my financial support allowing me to continue my degree and research, with the CUBIT group at Sandia National Laboratories supporting the early mesh optimization and boundary-layer meshing work. The University Hospital of Northern Norway and SINTEF in Norway provided three patient-specific cerebral aneurysm models.

I also want to thank my committee members Dr. Shelley Anna and Dr. David Vorp. They made sure this work was as grounded as it could be in the clinical world and not just a computational exercise. That reminder has only strengthened my belief that one needs to approach any work with an interdisciplinary mindset and group to work with. Dr. Anna was also my undergraduate research advisor. Without you I wouldn't be where I am today, thanks for always being willing to take time to answer questions and share your books.

To my labmates in the Computational Engineering and Robotics Lab (previously CIEL) and the Computational Biomodeling Lab. You were always there to bounce ideas off of and learn from; I can't thank you enough. You're brilliant people and it's been a pleasure to get to know you all. I hope I've returned a fraction of what you've done for me.

I couldn't have done any of this without my parents, sister, family, and friends. They have all allowed me to complain when I was frustrated, talk through a problem even when they didn't understand half of it, and joyfully share in progress made. I've remained sane because of you all; even having been in school my entire life. I love you all.

Thank you!

Contents

List of Tables

List of Figures

Chapter 1

Introduction

Cerebral aneurysms (CAs) are an enlargement of a brain blood-vessel due to a weakened wall and can pose significant health risks and computational simulations have been thus utilized to help doctors in understanding them. The rupture of a CA is difficult to predict and has a much more varied outcome when compared to the larger, abdominal aortic aneurysm. Some victims may suffer no complications, while for others it is fatal. If a CA ruptures, there is a 40% chance of mortality within 24 hours and an additional 25% chance of death due to complications within the next 6 months [1]. Being able to better predict the growth and failure of the vessel wall or, in the future, the outcome of surgical procedures, could significantly decrease the mortality rate of patients with aneurysms. However, the wall-thickness and material properties are very difficult to obtain experimentally, leading to most computational simulations using walls with uniform thickness and constant material properties. In order to provide more accurate patient-specific simulations a more accurate wall-model need to be generated.

1.1 Problem Statement

In the past few decades, simulating aneurysms has not only become possible, but is entering the phase where doctors can use them as a tool in predicting rupture. Cerebral aneurysms are an enlargement of a blood vessel due to a weakened wall, and can occur anywhere in the vascular system of the brain, but are most common around the Circle of Willis. As an aneurysm develops, the vessel wall will change in both its thickness and material properties;

however, accurately measuring *in situ* the thickness and material properties is difficult. Therefore most computational models adopt a wall with uniform thickness and constant material properties; though there are a few researchers who have begun looking at variable wall models [2,3,4]. Even though the simulation of cerebral aneurysms, through computational fluid dynamics (CFD) or fluid-structure interaction (FSI), is of critical importance, the lack of adequate thickness and material information in modeling will produce the wrong results.

While aneurysm pathogenesis is not fully understood, the initial growth is typically very rapid [5]. A reduction in the wall shear stress is one of the primary causes for the weakening of the vessel wall [5,6,7]. As the cerebral aneurysm wall is stretched, the primary, load-bearing component becomes the collagen layer as the elastin and smooth muscle cell layers degrade [8,9,10,11,12]. Scott *et al.* discovered that arterial tissue, after high-strain loading, loses the linear-elastic region in the toe of its stress-strain curves [8]. An increase in collagen growth is seen in regions of high strain in order to reinforce the vessel wall and attempts have been made at modeling this growth and remodeling through modified finite element methods [13,14,15,16]. The additional mass of collagen may thicken the aneurysm wall by a significant margin. However, there is likely little change in the mass during the initial, rapid formation of the aneurysm. While the thickness profile may vary over the cerebral aneurysm dome [17], the average thickness of the dome decreases to 50-100 μm [7,18]. Additionally, even with the potential for a thicker wall, the aneurysm itself is fundamentally weaker. In a sample of 125 ruptured intracranial aneurysms, 84% ruptured near the apex of the aneurysm dome, the fundus, while only 2% occurred at the neck [19]. To capture how these physiological changes affect the underlying stresses, one needs to

create the geometry of a patient's aneurysm from medical images and run computational fluid dynamic (CFD) or fluid-structure interaction (FSI) simulations.

The profile of an aneurysm can be found through segmentation of medical image data. By selecting the vessel wall within an image set, a discrete model of the aneurysm is generated. An isosurface of that model is then smoothed to yield the shape of the aneurysm. Closing the surface provides a volume that can be meshed for fluid analysis and by picking a thickness value the vessel wall can be modeled for structural simulations. However, outside of toy problems, a uniform wall thickness is almost always chosen.

Once an aneurysm has been modeled, it is meshed and prepared for analysis. Boundary and loading conditions are applied to mimic the environment and simulate the velocity and pressure conditions the aneurysm experiences. A CFD simulation provides a numerical solution to the Navier-Stokes and energy equations for a given domain and boundary conditions. This provides velocity and pressure profiles only for the blood flow within a rigid domain. To calculate the wall stresses of a flexible domain, or the creep of a stent after surgery, fluid-structure interaction (FSI) analysis is needed. FSI combines both finite element analysis (FEA) and CFD by passing the requisite information between both solvers. Since the pressure on a vessel wall changes as blood pulses through the vessel, this information is given to the structural solver and causes the wall to deflect. This altered domain is then passed back to the fluid solver and the process repeats.

The missing link between generating the profile of an aneurysm and running the analysis, is solving for a physically meaningful wall thickness and determining the material-direction of the vessel tissue. A doctor will not rely on an analysis if the results vary by an order-of-magnitude due to poor models. In order to provide increasingly precise, patient-

specific simulations, not only does the geometry for the fluid domain need to be created and accurate boundary and loading conditions applied, but the creation of a more accurate wall model needs to be accomplished as well.

The reason this thesis focuses on cerebral aneurysms, as opposed to including abdominal aortic aneurysms (AAAs), is because of the differences in pathogenesis and structure between the various aneurysm types (see Section 2.1.2). While it is our belief that the presented methods are easily extendable to abdominal aortic aneurysms, the fact that AAA walls become thicker, due to inflammation and neointimal proliferation, needs to be considered. If ignored, this distinction could further confuse the applicability of the proposed methodology to any aneurysm. However, regardless of the wall thickness, abdominal aortic aneurysms still weaken as they grow and need to be represented by an appropriate wall model.

1.2 Solution Approach

As a solution to improving analyses for cerebral aneurysms, this thesis presents the following work:

1. The development of an algorithm to determine an equivalent wall thickness for cerebral aneurysms. This entails moving the mesh from a healthy, blood-vessel model onto an aneurysm model and ensuring the deformed mesh is physically meaningful.
2. The extension of a medial-ball based sizing function to improve element sizing for prismatic meshing of the boundary-layer region in fluid domains. This

prevents mesh fronts from overlapping and helps to automate the meshing process.

3. The development of a new algorithm to predict material anisotropy for FSI simulations. This is accomplished by extending the deformation algorithm to add the tissue material-directions from the healthy model and moving them onto the aneurysm.

The focus of this thesis is primarily achieved through the creation of an *equivalent* wall thickness for patient-specific cerebral aneurysms. As the vessel wall weakens over the aneurysm dome, both the material strength and wall thickness changes. When performing a computational simulation, the weakened wall of an aneurysm can be captured through a thinning of the model wall and will yield more accurate analyses than is currently possible. The addition of a sizing function for boundary-layer meshing improves the adaptability of current advancing front methods (AFMs) for models with disparate feature sizes. This will reduce the user control needed to mesh the fluid domain by preventing overlapping of mesh fronts and increasing the usability of prismatic elements in these meshes. The algorithm used to determine the equivalent wall can be extended to find the anisotropic material-directions over the aneurysm dome, which will influence with thickness distribution and allow the material directions to be used in simulations.

Properly modeling the aneurysm wall is crucial to the success and accuracy of any simulation. Due to the difficulty in calculating the thickness from image data, most simulations approximate the wall with a constant value. The few that do use a variable wall-thickness rely on estimations from literature or smoothing functions. The presented

algorithm calculates the wall-thickness by deforming the mesh from a healthy blood-vessel model and mapping it onto an aneurysm. Using surface parameterization and spring-relaxation techniques, the final mesh gives a physically meaningful approximation of how the blood-vessel deformed. The stretching of the individual mesh elements can be used to predict the local deformation of the vessel and calculate an equivalent wall thickness. This algorithm needs to be flexible enough to accommodate new research into the pathogenesis of cerebral aneurysms and be able to adjust the wall thickness accordingly.

Prismatic elements can increase the flexibility of AFMs by reducing the number of elements required to capture the boundary-layer region and by better aligning elements in the flow direction. A common problem, however, is the overlapping of fronts from competing surfaces. This is particularly problematic in domains with disparate feature sizes, where fronts that fit in the bulk of the model are too large for smaller regions. The proposed method solves the overlapping issue by limiting the growth of the boundary-layer mesh in certain regions with a medial-ball based sizing function [20,21]. The sizing function is stored on a background octree and is determined by the largest sphere that can fit at any location. Additional smoothing is used to ensure a gradual transition between the mesh regions, and to ensure that no element tangling occurs. By using the medial-ball, the boundary-layer mesh will only shrink in regions of potential overlap while preserving the desired number of layers in the mesh. This means that a minimum number of elements are still present where the flow becomes constricted, while keeping the user-desired parameters for the rest of the domain.

Determining a method to properly capture the material directions for an aneurysm model will provide more an accurate wall-thickness from the proposed mesh deformation.

The material directions can then be used within a FEA or FSI solver to improve the accuracy of stresses. While the material directions are currently being found with a centerline, the *true* directions are not guaranteed to be aligned so conveniently. The presented method for determining the directions of anisotropy is to use the principle-curvature directions of the healthy model to determine the axial and circumferential directions. These should be closely aligned with the material directions and can be moved those through the mesh deformation algorithm in a similar manner to the thickness. As with the mesh deformation, this algorithm needs to be able to start with material directions not aligned with the axis as more information becomes available.

1.3 Implementation and Simulations

The algorithms developed for this thesis have been implemented within and make use of the tetrahedral meshing routines from CUBIT, a standalone meshing toolbox developed at Sandia National Laboratories. ANSYS® v12.0 and ANSYS®, CFX™ v12.0 were used to perform the FSI simulations.

1.4 Papers/Presentations

1.4.1 Papers

1. E. Johnson, Y. Zhang, and K. Shimada, "Using Parameterization and Springs to Determine Aneurysm Wall Thickness," *Proceedings of the 18th International Meshing Roundtable*, Salt Lake City, UT, USA: Springer, 2009, p. 397-414.
2. E. Johnson, Y. Zhang, and K. Shimada, "Estimating an Equivalent Wall-Thickness of a Cerebral Aneurysm through Surface Parameterization and a

Non-linear Spring System," Submitted to International Journal for Numerical Methods in Biomedical Engineering, May 2010.

3. E. Johnson, M. Brewer, S. Yamakawa, S. J. Owen, and K. Shimada, "Growing a Prismatic Boundary-Layer Mesh Using a Medial-Ball Based Sizing Function," To be submitted to Engineering with Computers, July 2010.
4. E. Johnson, Y. Zhang, and K. Shimada, "Determining Anisotropy for Cerebral Aneurysms," To be submitted to International Journal for Numerical Methods in Biomedical Engineering, October 2010.

1.4.2 Presentations

1. Poster, Generating an All-Hexahedral Boundary-Layer Mesh, 17th International Meshing Roundtable, Pittsburgh, PA, October, 2008.
2. A Method for Generating a Hexahedral Boundary-Layer for CFD Simulations, CUBIT External Review, 17th International Meshing Roundtable, Pittsburgh, PA, October, 2008.
3. Aneurysm Wall Thickness Estimation with Surface-Mesh Parameterization and Non-linear Springs, 18th International Meshing Roundtable, Salt Lake City, UT, October, 2009.

1.5 Contribution

This thesis will have four principle contributions:

1. A mesh deformation algorithm that provides aneurysm wall thickness information.
2. A meshing algorithm that incorporates feature sizes to prevent the overlap and tangling of elements.

3. An algorithm that provides material-directions for use in mesh deformation and finite element analysis.
4. An implementation of the above algorithms so they can be used on patient-specific aneurysms.

1.6 Thesis Overview

Chapter 2 gives an overview of the human cardiovascular system along with the anatomy and the currently known pathogenesis of cerebral aneurysms, along with a background into work previously performed in regards to modeling and simulating aneurysms. It then continues by specifically discussing past research on individual techniques used within this thesis: geometric smoothing, surface parameterization, mass-spring model deformation, and boundary-layer meshing. Chapter 3 discusses the process of deforming the mesh of a healthy, blood-vessel model onto an aneurysm model. Chapter 4 presents a new sizing function for use with meshing the boundary-layer region of fluid domains. FSI simulation results showcasing the advantages of the methods are discussed in Chapter 5. Chapter 6 discusses the extension of the mesh deformation into including anisotropy and Chapter 7 concludes this thesis.

Chapter 2

Literature Review

2.1 Human Cardiovascular System

The human cardiovascular system moves blood throughout the body, bringing in nutrients and removing waste as it travels through the arteries and veins, respectively. The periodic contraction and relaxation of the heart drives the blood flow and will speed up when a person is active or slow down when they rest. This creates a cyclic pressure profile, where the ratio between the high, systolic, and low, diastolic, pressures in the blood vessels is a person's "blood pressure". The pressure profile is partially influenced by how much the vessel wall distends under load and will change as plaque and calcification, among other diseases, alter the properties of the wall. When there is an increase in the pressure the tissue will stretch and then subsequently relax as the pressure wave travels downstream, passively pushing the blood further through the rest of the body. Since the health and shape of the vessel wall will determine how much it distends, and thus the stresses the wall experiences, they play an important role in how the blood flows through the system and the likelihood of an aneurysm to rupture. In order to perform more realistic simulations, a better understanding of the vascular system and the pathogenesis of cerebral aneurysms is required.

2.1.1 Human Vasculature

The Circle of Willis supplies blood to the brain and is fed by the internal carotid arteries, in the neck. This ring is located on the underside of the brain and branches into smaller and smaller vessels to provide the entire brain with oxygen. The largest branch off of the circle is

the basilar artery, and while aneurysms can appear anywhere in the human vasculature, they seem to occur most often on the largest arteries and near a split, or bifurcation. This may be due to the blood flow impinging into the wall directly, but contradicts the notion that aneurysms grow in regions of low wall shear stress [22,23,24,25].

Blood vessel walls are flexible bodies comprised of three layers: the (1) tunica intima (innermost), (2) tunica media (middle), and (3) tunica adventitia (outermost), seen in Figure 2-1(a) [5,8,17,18], and provide the structural support and elasticity required to continually distend and relax as the blood pulses through the body. The blood flows in the lumen and the intima is a membrane of endothelial cells lining the artery wall. Composed of elastin and smooth muscle cells, the media allows the vessel to recover after being distended, while the adventitia is made up of layers of collagen and fibroblasts, the latter of which control the growth of collagen [16]. Vessel walls have a thickness between 15-20% of the local vessel radius, which means the wall of the basilar artery is approximately 300 μm thick [6,7,17,26].

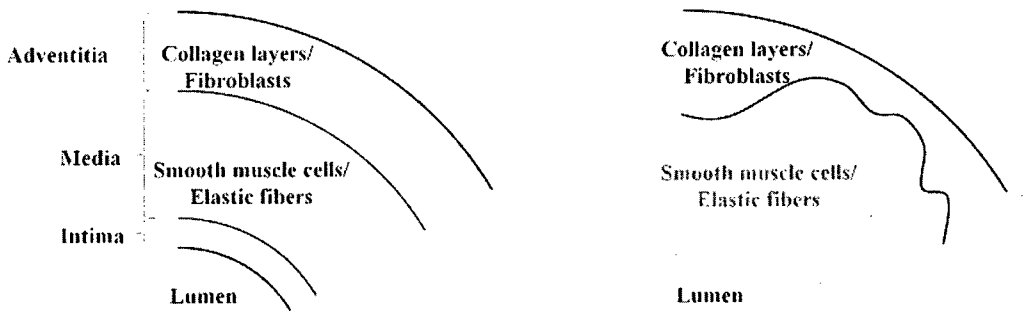

Figure 2-1: Schematic of a healthy and aneurysmal vessel wall.

Vessel walls undergo a couple billion loading cycles during the average human lifespan. This is achieved by having a wall that can elastically recover from small displacements and is aided by a continual growth of new material. The elastin in the media is a linear-elastic material preventing the vessel from deforming plastically under normal conditions, i.e. small strains [8]. Collagen fibers are a non-linear material that supply the bulk of the structural support for the blood vessel and is typically not stretched a significant amount [8,16,27,28]. Under an extreme load, this material non-linearity ensures the stiffness increases as the collagen is further stretched, distributing the load over progressively larger areas.

A unique feature of the vessel wall is that the tissue exhibits clearly anisotropic material directions, i.e. it stretches more in one direction than another under the same load. The adventitia is made up of five to fifteen layers of collagen, with the fibers in each layer being parallel [5,13]. The outermost layer supports approximately 58% of any load on the wall and is oriented in a nearly axial direction [29,30,31,32]. The second principal direction is circumferential (orthogonal to the first) and is found in the innermost layer of collagen. All of the remaining collagen layers transition in their orientation between the two primary directions. The anisotropy arises from collagen being a linear structure, resulting in it being strongest along its length and weakest in the perpendicular direction. Unlike most materials, the linear nature of collagen means the material directions will remain perpendicular, regardless of how it is stretched. The final anisotropy is actually offset from the axial direction by a small degree of rotation, as each layer contributes a small amount to the overall structure, but it is still considered predominately axial [32,33,34,35,36].

2.1.2 Pathogenesis of Cerebral Aneurysms

It is still not fully understood as to what causes aneurysms to form and rupture. The initial growth is considered to be rapid, with the lower end on the order of three to four months, and is has a significant risk of rupturing [5,37]. The aneurysm then reaches a steady-state size where it will remain indefinitely or continue to grow, but at a significantly slower rate. The critical size for intracranial saccular aneurysms (ICAs) is somewhere between 3-5 mm in diameter and is unlikely to rupture when smaller [17,37]. Non-critical ICAs may still "crack" and bleed, causing hemorrhaging and a subsequent strengthening of regions of the wall with scar tissue.

There does appear to be a link between aneurysm formation and regions of low wall shear stress [24]. The reduction in shear would diminish a primary direction for the tissue to align with and reduce the oxygen the region receives causing the extracellular matrix within the media to breakdown [38,39]. In abdominal aortic aneurysms this breakdown coincides with neointimal proliferation (a rapid growth of endothelial cells in the intima) and inflammation of the vessel tissue, which further weakens the wall and may result in it becoming thicker as the aneurysm grows. In contrast, the growth of cerebral aneurysms appears to be more rapid, with the inflammation and proliferation arising after the aneurysm has been formed and about to rupture [10,40,41,42].

Regardless of what initiates the growth of a cerebral aneurysm, the aneurysm wall "loses" the tunica media and is at that time only supported by the collagen layers of the adventitia. Scott *et al.* demonstrated this loss during pressure loading of healthy cerebral arteries to 200 mm Hg, where, after a few loading cycles, there was no longer a linear elastic region in the tension-displacement curve, and is reproduced in Figure 2-2 [8]. Even though

the "toe" of the plot disappeared, the non-linear regions of the curve remained virtually parallel. The offset can be accounted for by the change in unloaded radius after the elastin no longer contributed to the structure.

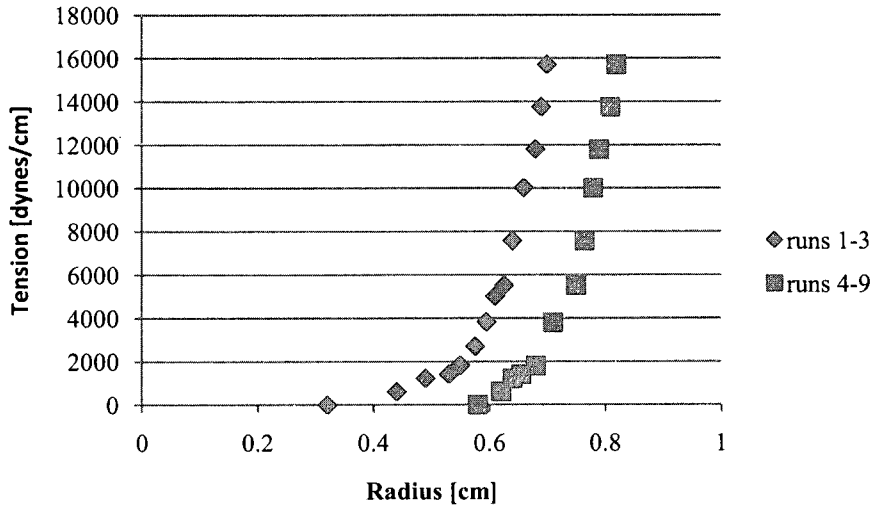

Figure 2-2: Plot of tension – absolute radius for arterial tissue, reproduced from [8]

While multiple equations exist for approximating the material model for blood vessel tissue [9,30,36], one of the most common is an exponential by Fung *et al* and captures the effect of the anisotropic properties [28,43]. Equation (2.1) is the resultant strain-energy equation, where ε_{zz} and $\varepsilon_{\theta\theta}$ are the axial and circumferential strains, respectively, and $a_1 = 2.5$, $a_2 = 0.46$, $a_4 = 0.176$, and $C = 2.9$ are material constants for the carotid artery [28,44]

$$W = \frac{C}{2} e^{a_1 \varepsilon_{\theta\theta}^2 + a_2 \varepsilon_{zz}^2 + 2a_4 \varepsilon_{\theta\theta} \varepsilon_{zz}} \tag{2.1}$$

The material limits also need to be known to represent the material response to a loading. During its initial growth the average wall thickness over the aneurysm dome decreases to 50-100 μm, relative to the 300 μm for a healthy artery [7,18]. MacDonald *et al.* used polarized light microsopy with four cerebral aneurysms to estimate a breaking stress of 0.73 to 1.9 MPa and found the ruptured wall thickness varied between 16--38 μm for their samples [32]. In work by Raghavan, AAAs from four cadavers were cut into strips and measured to determine a tensile yield stress for the vessel-wall tissue [45]. The ultimate stress had an average of 1.27 MPa, but varied across the samples from 0.36 MPa to 2.35 MPa.

As stated previously, collagen is continually being replaced in a process Humphrey and Taylor title "growth and remodeling" [5]. The body limits the chance for failure due to fatigue by giving collagen a half-life of approximately 70 days. To ensure fatigue does not become a problem as loading rises, the half-life of collagen is shortened [5,13,15]. This removes the chance any one fiber experiences the cyclic loading for too long. To further decrease the internal loads in the vessel wall, as fibroblasts create new collagen, they will contract the nearby fibers to add a prestress to the new material, distributing the load more evenly [27]. For cerebral aneurysms this means that after the rapid initial growth, where little to no mass is added, the body will try and control the aneurysm growth and strengthen the wall by adding new collagen. This is seen in the cross-sections taken by Suzuki and Ohara, where the wall becomes thicker only after an ICA grows larger than its critical diameter [17].

2.1.3 Aneurysm Modeling and Simulations

In order to analyze a patient-specific cerebral aneurysm four things need to be done: (1) an image of the aneurysm needs to be taken, (2) a 3D model of the aneurysm needs to be created, (3) the aneurysm model needs to be meshed, and (4) a simulation needs to be

performed with proper boundary and loading conditions need to be applied. The imaging provides a shape for the model, which can then be meshed; though for cerebral aneurysms the imaging is only suited for capturing the fluid domain and not the wall of the aneurysm at this time. The boundary and loading conditions determine under what circumstances the aneurysm is being looked at, e.g. at rest, while a person is running, etc.

2.1.3.1 Imaging Techniques

Imaging aneurysms is most often accomplished through three methods: computer tomography (CT), magnetic resonance (MR) imaging, and ultrasound. Ultrasound, however, is not appropriate for cerebral aneurysms. If a contrast dye is used to enhance the image, the first two are referred to as CT and MR angiography. CT scans use X-rays to capture the region of interest and have a resolution of about one millimeter [46]. Higher doses of X-rays can be used to achieve sub-millimeter dimensioning, but pose a greater risk to the patient. MR imaging, on the other hand, uses magnetic fields to align hydrogen atoms within the cells in order to capture soft-tissue. This procedure often takes significantly longer than CT imaging, but provides both a higher contrast between tissues and a higher spatial resolution. Park *et al.* show that double inversion recovery black-blood sequence (BBDI), a technique for MR angiography where an inverted pulse "removes" the blood from the image to increase the contrast in the vessel wall, can be used to improve the quantification of wall thickness in cerebral aneurysms [47]. An enhanced rendering of a 512x512x80 brain MRA can be seen in Figure 2-3. This technique is able to achieve resolutions of 0.48x0.58 mm for 3 mm slices. Ultrasound imaging emits high frequency waves and is able to reproduce an image based on the reflected pattern that is returned. This method of imaging is very adaptable and portable, but is acknowledged to produce images with significant noise.

Nicholls used ultrasound scans from 160 patients with AAAs to determine if there was a correlation between aneurysm size and chance of rupture [48]. Intravascular ultrasound (IVUS) has been used to image coronary arteries with 0.2 mm accuracy [49]. However, as a result of the equipment being inside the artery, this technique is not usable for smaller vessels.

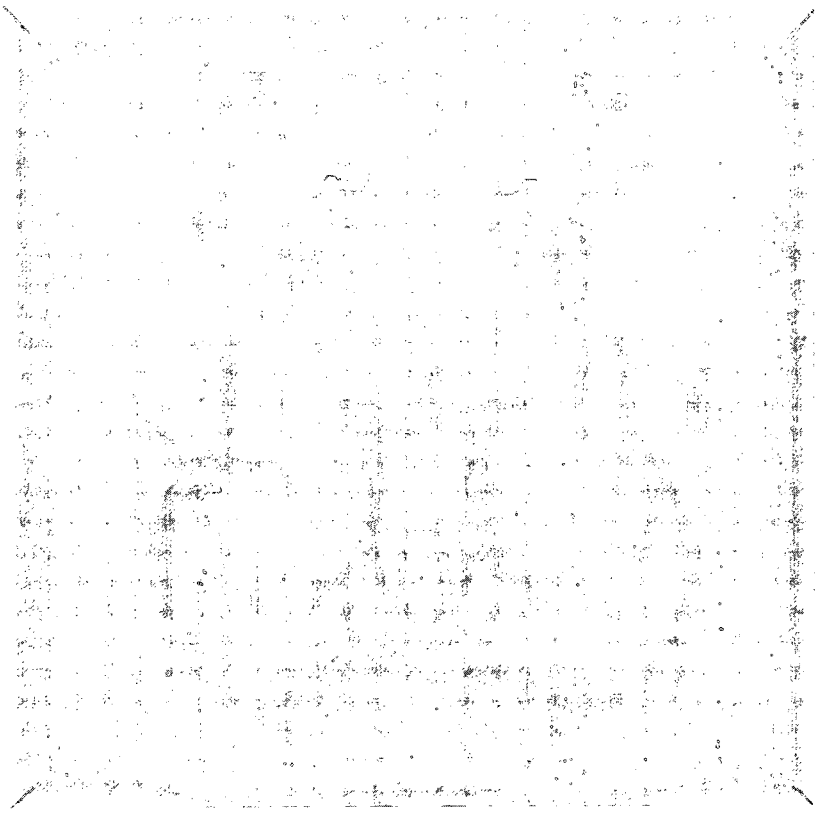

Figure 2-3: Enhanced, volume rendering of a brain MRA

In every instance, the image resolution is of the same length scale or larger than the minimum wall thickness at a rupture site. Even though walls of AAAs can be seen in medical images, an exact thickness is hard to determine for the thinnest regions. Since the image is

comprised of discrete data, only a bound on the thickness can be guaranteed and interpolation has to be used for any approximation. This process becomes more difficult yet as the vessels become smaller in the brain. Additionally, the orientation of the vessel wall relative to the image direction can play a significant role in the perceived wall thickness. Steinman *et al.* show the thickness calculated from an image can be exaggerated by over 50% larger [50]. Figure 2-3 demonstrates that for a single image slice the perceived thickness, B, can be significantly larger than the actual wall thickness, A.

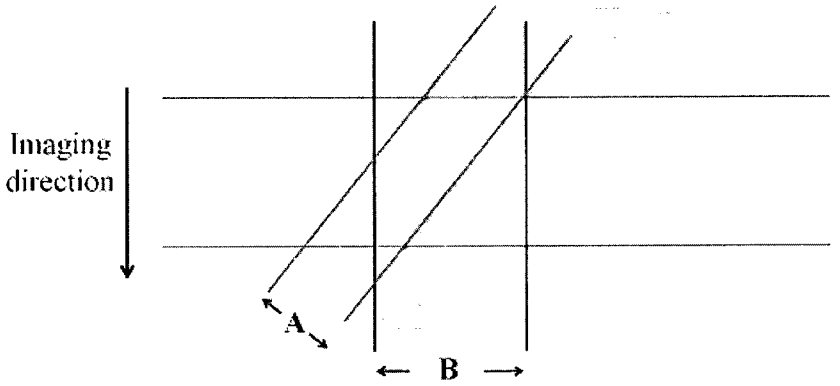

Figure 2-4: Wall thickness as perceived by imaging techniques

2.1.3.2 Modeling

The surface of an aneurysm can be extracted from the image data by segmentation. Segmentation is a method which tries to group "like" regions of an image together so it can later be separated out. One of the most common methods to segment an image is region-growing, with the general flow seen in Figure 2-4 [7,51,52,53,54,55,56,57]; however others, such as thresholding [24,58,59,60,61], watershed method [62], neural networks [63], deformable models [64], and tracing of the image [65], can be used. In region-growing, a user "seeds" the image by selecting a handful of points and classifies them as being regions of interest are or not. Pixels neighboring a cluster are added to the region if they meet criteria

based either on the intensity gradient or a threshold. This is repeated until every pixel has been visited. All of the clusters determined to be a part of the aneurysm are combined and yield a rough outline of the blood vessel. While there is a push to automate this part of the process, significant user input is still required for proper classification and segmentation.

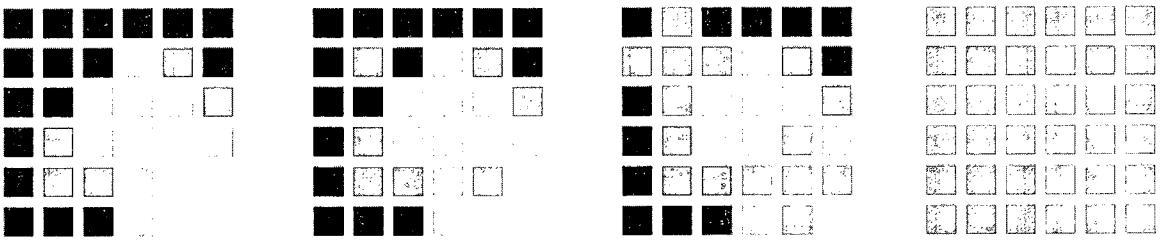

Figure 2-5: Workflow for segmenting image data by region growing

Since the segmented data is still a collection of discrete voxels the shell is a stair-step surface and an isosurface needs to be extracted to produce a smoother model. The most popular method for generating an isosurface is marching cubes [7,51,52,53,54,57]. Here, a polygon is created within each voxel that coincides with the desired image intensity, or isovalue. The polygon is formed by interpolating the points along each edge for an isovalue. All of the polygonal surfaces are patched together to form the isosurface. Additional smoothing may be required to improve the surface mesh or remove any noise still present. NURBS (NonUniform Rational B-Splines) are frequently used to create a final, smooth surface [51,66], though Laplacian smoothing [24], Hermite-interpolation [65,67], and geometric flow techniques [68,69,70,71] have also be used.

Creating a three-dimensional model of the aneurysm wall requires the addition of wall thickness to the surface model. The image data is sometimes used [47,63] to measure the wall thickness, but more often than not, is kept constant [7,30,53,57,58,59,60,61,66,72]. Scotti does use a linear interpolation, which changes from the maximum thickness to the minimum value of 0.24 mm found by Raghavan for AAAs [45], along a straight model to add a variable thickness to the model simulated [73,74]. However, this is not usable for more complicated models, and applying a similar approach to patient-specific models would still not be using the correct thickness values. Bazilevs *et al.* use a smoothing technique to create a wall that is a uniform 20% of the radius over the entire domain [6]; however, this means the thickness of the aneurysm is the same as if the vessel were healthy. Torii *et al.* set the healthy artery to be a constant and use the average 50 μm as a constant over the ISA dome [7]. While processing the image data produced by the BBDI, Park *et al.* were able to determine the thickness for some cerebral aneurysms [47]. Out of fourteen patients, the wall thickness was only able to be found for ten, and it was not possible to determine the value at every location. The mean wall-thickness of the parent artery for the ten patients was 0.59 ± 0.11 mm. The dome of the aneurysm was detectible in only five out of the fourteen patients, with a mean wall-thickness of 0.46 ± 0.05 mm. Martufi *et al.* calculated the wall thickness for an AAA by subtracting two image sets from one another and showed a maximum difference of 7.8% between the predicted thickness and the measurements taken by Raghavan [45,63]. The first image is created using a neural network and includes everything within the aneurysm, while the second, using histogram based segmentation, should exclude the aneurysm wall. Though not every part falls within an area of "detectable

thickness", three-dimensional interpolation is used to approximate the wall for the entire model.

2.1.3.3 Simulations

CFD and FSI analyses are used to study the blood flow and the wall stresses and displacements through the vasculature [2,24,30,53,57,61,65,66,72,73,74,75,76,77,78,79]. Before it can be used in a simulation, a model needs to be meshed (discussed in more detail in Section 2.4) and any material properties and boundary and loading conditions need to be applied. However, the material properties cannot be found *in vivo* for patient-specific simulations. As a result most simulations use constant, isotropic material properties in addition to the uniform wall thicknesses.

Simplifying the material, along with the thickness, removes complexity from the simulation and decreases simulation time. The vascular system is incredibly complex and most approximations are to deal with the lack of adequate information, while still trying to make forward progress in understanding it. Linear-elastic, isotropic materials are commonly used because of their simplicity [51,53,66,73,74,75,76]. A linear material responds linearly-proportional to the forces acting upon it, and an isotropic material responds the same in every direction. Under small strains this is how healthy vessel tissue reacts. Unfortunately, during the growth of an aneurysm, the elastin is stretched beyond its limits. Non-linear, isotropic materials are being used with increasing frequency as our understanding of blood-vessel tissue improves and as computational power increases [57,61,66]. Non-linear, anisotropic models are just starting to be used, but rely on approximations of the material directions as being distinctly axial and circumferential [30]. The directions are currently found by creating a centerline for the aneurysm to approximate the axial direction, with the

circumferential being orthogonal to the surface normal and the centerline [30,34,36,80]. The addition of anisotropy is difficult and is discussed further in Chapter 6.

Some of the boundary and loading conditions can be determined *a priori.* Though usually approximated for general simulations, a patient-specific velocity profile can be found via pulsed-doppler ultrasound [81]. This provides a repeating waveform that is set as the inlet boundary-condition. The pressure profile can either be imposed on the outlet with a phase-lag from the velocity profile [74,78] or set as a resistance to the flow to better approximate the fractal branching of the vessels in the brain [82]. For FSI analyses, the ends of the blood-vessel can be fixed or allowed to freely slip along a plane [6]; they may also be given a small tensile force to approximate the stresses applied by the adjacent structure [73]. There can be an additional external load placed on the vessel wall to approximate the intracranial pressure, though more than a general pressure is hard to guess due to the response of the brain being deformed via the aneurysm.

When running simulations, the vessel walls are either rigid (CFD) or compliant (FSI). Torii showed the impact of both the cerebral aneurysm shape and the use of a rigid versus a flexible wall on the flow profile and stress results [78]. Using an assumed 0.3 mm uniform wall thickness, Torii *et al.* found a 20% decrease in wall-shear-stress when using compliant, instead of rigid, walls. A similar result was found by Bazilevs through a series of cerebral aneurysm models [2]. Again these models assumed a uniform wall thickness. Using a flexible wall, Scotti *et al.* showed upwards of a 400% increase in von Mises stress when a variable wall-thickness is used over its uniform wall-thickness counterparts [73,74]. The thickness of the wall used for their aneurysms is a predetermined range that falls within the measured data from Raghavan [45].

The use of simulations is also being practically applied toward treatment of aneurysms. As an example, the placement of stent-grafts can be simulated to monitor their migration and efficacy over time [61]. As a stent moves, its efficacy decreases and may become dislodged. By simulating the best location for a stent, the likelihood of performing a repeat surgery is dramatically decreased. Silicone models are also being created from image data to improve physical experimentation [58,60,83]. This may provide valuable data to validate simulated results against, though they are limited by the material and wall thickness they use.

An alternative method for a structural simulation of the aneurysm wall is to include the growth and remodeling of the collagen in the FEA solution [13,14,16,84]. This framework is just beginning to be developed and introduces a rate of growth allowing mass to be added to the wall as it is strained in order to stabilize the size of the aneurysm. When the growth rate is too small, the aneurysm will grow unbounded; otherwise it will reach its steady-state diameter somewhere between 3-100 years [13]. During this time the amount of collagen that can be added to the fundus increases by 240%. It needs to be noted however, that at this time this framework: (1) has only been used on modified and idealized geometry, thus it is not usable to match patient-specific geometries, (2) does not take into account any stretching of the collagen that would decrease the thickness, and (3) does not provide a physically realizable model that can achieve the smallest thicknesses seen at the site of rupture.

2.2 Surface Parameterization

Parameterization is used frequently for texturing and surface decimation of models in video games and movies [85,86,87,88,89,90]. It takes three-dimensional geometry and projects it onto a planar (or a series of planar) domain(s). There should be a one-to-one relationship

between any point on a map to its parent surface. Sheffer wrote a survey in 2006 detailing much of the work on linear mapping algorithms [88]. Most of the traditional mapping schemes will only move elements between convex domains with no holes, and depending on the parameterization scheme, different guarantees can be made about the quality. Conformal mapping, for example, guarantees angle preservation between the elements on the parent mesh and the map [91,92].

For more complex domains, i.e. closed solids or n-manifold surfaces, it is common to partition the shape into smaller, manifold regions, or atlases [88,89,93]. These methods create an atlas that correctly links part of a surface to an individual map. Partitioning, however, is not ideal for the target application of this paper as defining identical regions between a healthy and aneurysm model would require extensive user interaction. Kim and Yin showed alternative methods for mapping multiply connected discs [87,90]. Kim *et al.* used Ricci flow to move a face with holes, for the mouth and eyes, onto an annulus in order to perform expression recognition [87]. Slit mapping was presented by Yin to show a linear solution to the same problem with the ability to set arbitrary boundaries to the inner and outer ring [90].

2.3 Mass-Spring Models

Model deformation is commonly accomplished through the use of mass-spring systems [94,95,96,97]. Using elasticity theory, a stiffness matrix could be created and solved to model and animate the deformation of rigid bodies [97]. However, this can become computationally expensive as the domain increases in complexity. Gudukbay showed solving local spring equations was a good substitute to the older methods and could still provide time-dependent deformations [96]. Both Chen and Cui have recent work for haptic feedback

with surgery simulations that utilizes mass-spring systems to provide displacement and force information to the user [94,95]. Provot makes use of non-linear springs to improve the accuracy and stability of large-strain deformations in rubber-like materials [98]. It should be noted that the blood-vessel tissue is constantly trying to repair itself, and while an aneurysm is growing, the walls are slowly becoming stronger as well. Kroon and Holzapfel have an finite element simulation that incorporates the growth and breakdown of collagen in the creation of a cerebral aneurysm [14].

2.4 Boundary-Layer Meshing

2.4.1 Overview of Advancing Front Methods

Advancing front methods (AFMs) are one of the most common algorithms to generate boundary-layer meshes because of their relative robustness and ability to easily generate anisotropic layers [99,100,101,102,103,104,105,106]. Proceeding from a surface mesh, elements are generated in layers as fronts march inward to fill the volume. Once opposing fronts meet, individual elements can be used to fill the remaining space, or more complex methods, like stitching elements together [107], can be used to connect the mesh. An illustration of meshing a domain with a quadrilateral AFM can be seen in Figure 2-5. Meshes that will be used for CFD simulations may use an AFM to create the boundary-layer mesh, and then proceed to another algorithm to fill the remaining space.

A common concern while using AFMs is when to terminate individual fronts in order to prevent elements from overlapping, *i.e. front-collision.* This is a particular issue for CFD simulations, where the meshes are typically characterized by layers of highly anisotropic elements adjacent to any walls in the fluid domain. These elements are stretched in the direction of the flow and capture the rapidly changing velocity within the boundary layer.

However, in regions where the distance between a set of walls is very narrow, there is a chance the mesh will overlap, or that too few elements are present to capture the flow properly.

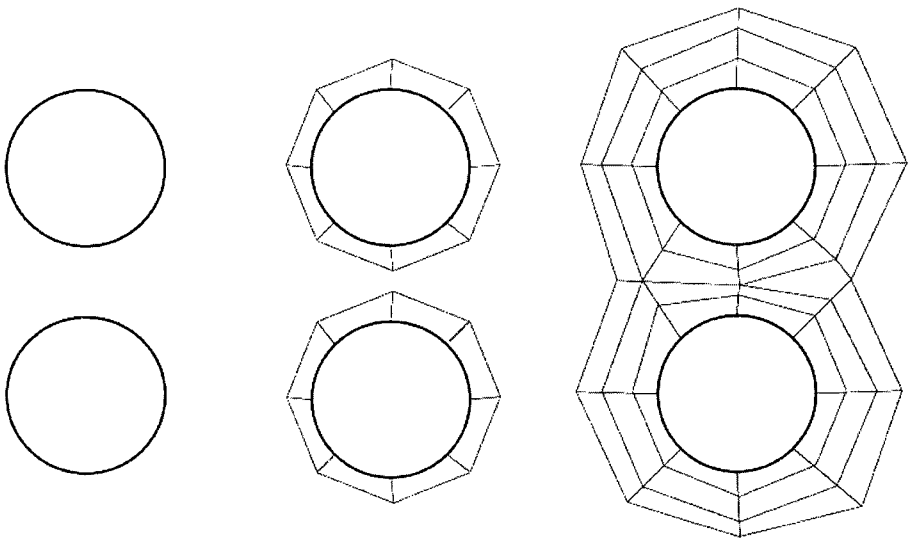

(a) Starting domain **(b) 1st layer from AFM** **(c) Continuation of AFM**

Figure 2-6: Illustration of advancing front method

Front collisions frequently occur when the domain has features of disparate size. In these cases the element are of the same or larger length scale as the features and prevent or limit the boundary-layer mesh from growing. This may yield fewer elements to capture a changing flow. Overlapping may also occur in regions of high curvature, where the radius of curvature is smaller than the desired boundary-layer mesh thickness.

In general, preventing overlapping fronts for AMFs has been solved using two methods: (1) shrinking the element, or (2) not placing an element. However this only works well for tetrahedral meshes, because it may not be possible to fill the remaining space with a single element type, like all-hexahedral meshing, or the complexity of the mesh and

algorithms substantially increase, *i.e.* meshes with multiple element types and ensuring enough room in the mesh for transition elements [108]. However, using anisotropic, prismatic elements can significantly reduce the computational cost during analysis by decreasing the degrees of freedom of the mesh. Additionally, prismatic elements are better suited for CFD simulations since their faces are more orthogonal to the flow than would be with a tetrahedral mesh [109].

2.4.2 Previous Work

Garimella and Shephard give an extensive account on creating a boundary-layer mesh with anisotropic tetrahedrons [99]. Layers of wedges are grown from a triangular mesh with a length determined through various specified parameters and a direction normal to the surface. If acute corners or near-geometry cause the boundary-layer to invert or overlap, the growth curves are first trimmed; if that fails, layers are locally removed. The elements are then subdivided into the tetrahedra to create an all-tetrahedral mesh. Khawaja and Kallinderis use a similar procedure to create a wedge-tet hybrid mesh [100]. As opposed to Garimella and Shephard, the wedges are not subdivided. Additionally, the boundary-layer mesh thickness is sized relative to the curvature of the geometry, being thinner in regions of high curvature. Like in [99], layers are removed if overlapping occurs.

Corners pose a particularly large problem in AFMs. If a corner is convex, then extruding the mesh can cause highly skewed elements. However, if a corner is concave, then there is a possibility the mesh will overlap. To improve convex corners while using an advancing front, Garimella [99] and Ito [102] recommend using multiple growth curves at nodes on edges and vertices. This not only reduces the shear of the elements, but can increase the orthogonality of element faces to the flow. As with removing elements from

layers, if the mesh is not all-tetrahedral it will require additional element types. Mesh enrichment [104,106] subdivides the mesh in outer layers to reduce the shear. At concave corners Shaw *et al.* and Chalasani et al. demonstrate a means to collapse the mesh in to increase the element quality and avoid tangling. Löhner and Cebral, however, use directional enrichment to improve the quality of the tetrahedral boundary elements at corners by removing all the elements within a specified distance of the surface and refilling it with isotropic layers of varying size [105]. While technically a constrained Delaunay algorithm, it moves from the interior of the domain toward the surface in a layered manner.

There are many methods to determine how thick the boundary-layer mesh should be. Instead of relying on the AFM, Krause et al. create an offset of the boundary for 2D electrical simulations of transistors [110]. Using a user-defined value, the regions next to the boundaries can be anisotropically meshed independently of the remaining space. Garimella provided multiple equations that could adapt the thickness based on its location on the surface. Using an adaptive approach, the boundary-layer mesh could match the theoretical growth of the boundary-layer on a flat plate [99]. Wang uses the weak solution to the Eikonal equation to determine the thickness of the mesh [103]. This will give the shortest distance from any point to the boundary.

An alternative to relying on a single mesh is to update the mesh from *a posteriori* information from the solution. Sahni *et al.* obtained more accurate wall shear stress (WSS) results by using an adaptive approach to improve an existing boundary-layer mesh [77]. Using the solution to generate tensors at the boundary-layer nodes, the anisotropy in the mesh could be changed to improve the solution.

Besides AFMs, octrees are another method for generating boundary-layer meshes. Octree methods are a way to subdivide a space in a grid-like manner; but unlike a full Cartesian-grid mesh, an octree only subdivides while capturing features, like the boundary. This reduces the total number of elements in the entire mesh, while producing the same boundary resolution. Using an octree mesh provides a significantly more structured interior mesh, but is typically thought to have poorer quality near the boundary. Zhang uses pillowing near the boundary to create higher-quality elements that are also aligned with the flow near the surface [52,79]. Isaksen *et al.* have used these meshes to run FSI analyses on cerebral aneurysms [57].

Chapter 3

Equivalent Wall Thickness

The quality of the model used in a simulation plays a crucial role in the results it produces. Dependent on the information required and the simulation being run, the model may need to suppress certain features, or add them. For simulating aneurysms, the geometry shape influence the blood flow and the stresses it exhibits on the vessel wall. Furthermore, as shown in [73,74], the wall thickness can significantly influence the results. Unfortunately, determining the thickness through image processing, especially for smaller vessels, does not appear capable of providing enough information.

This chapter presents a method to calculate the aneurysm wall thickness without relying on the image data. By deforming the surface-mesh from a healthy blood-vessel into the aneurysm model, the wall thickness is directly related to the area change in an element. As can be seen in Figure 3-1, the algorithm has three principle steps:

1. Deform the mesh from the healthy model, S_0, onto the patient-specific aneurysm model, S_1, through surface parameterizations;
2. Relax the nodes of the mes S_2h, , according to a non-linear spring model;
3. Calculate the thickness at each node as a result of the deformation of the mesh.

By deforming the mesh through a combination of parameterization and spring relaxation, the resultant mesh, S_3 , will both match the shape of the aneurysm and provide a solution that mimics the elastic, stretching nature of the blood vessel wall. It is assumed that

a negligible amount of mass is added to the wall during the initial aneurysm growth, and any inflammation or neointimal proliferation, which would weaken the wall, can be characterized by the thinning wall.

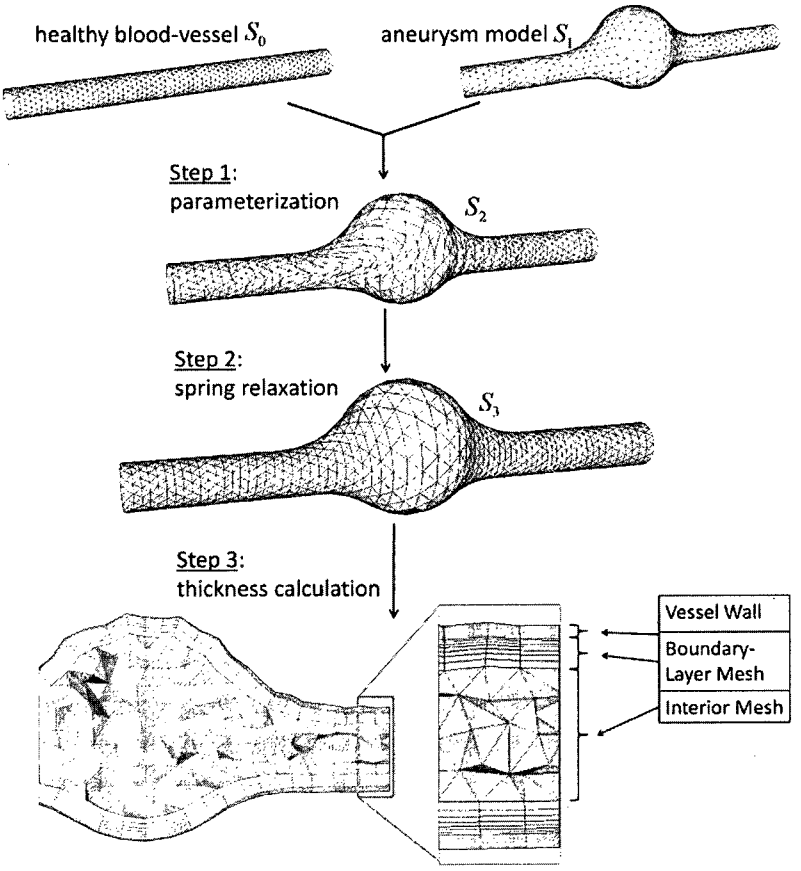

Figure 3-1: Overview of mesh deformation

3.1 Creating a Surface Parameterization

3.1.1 Moving Mesh between Models

Figure 3-2 shows the process of deforming one surface onto the other with the same topology, where a node on the healthy surface moves to its new location on the aneurysm model. First, the healthy and aneurysm surface-meshes are parameterized onto planar discs

of the same size, Q_0 and Q_1. Second, nodes on these discs are moved until the outlet-boundaries from one map line up with the corresponding ends in the other, its *pair*. Third, each node x_0 on the healthy model finds a location x_2 on the aneurysm surface through a barycentric coordinate system. The set of x_2 will form the deformed model S_2 in Figure 3-1.

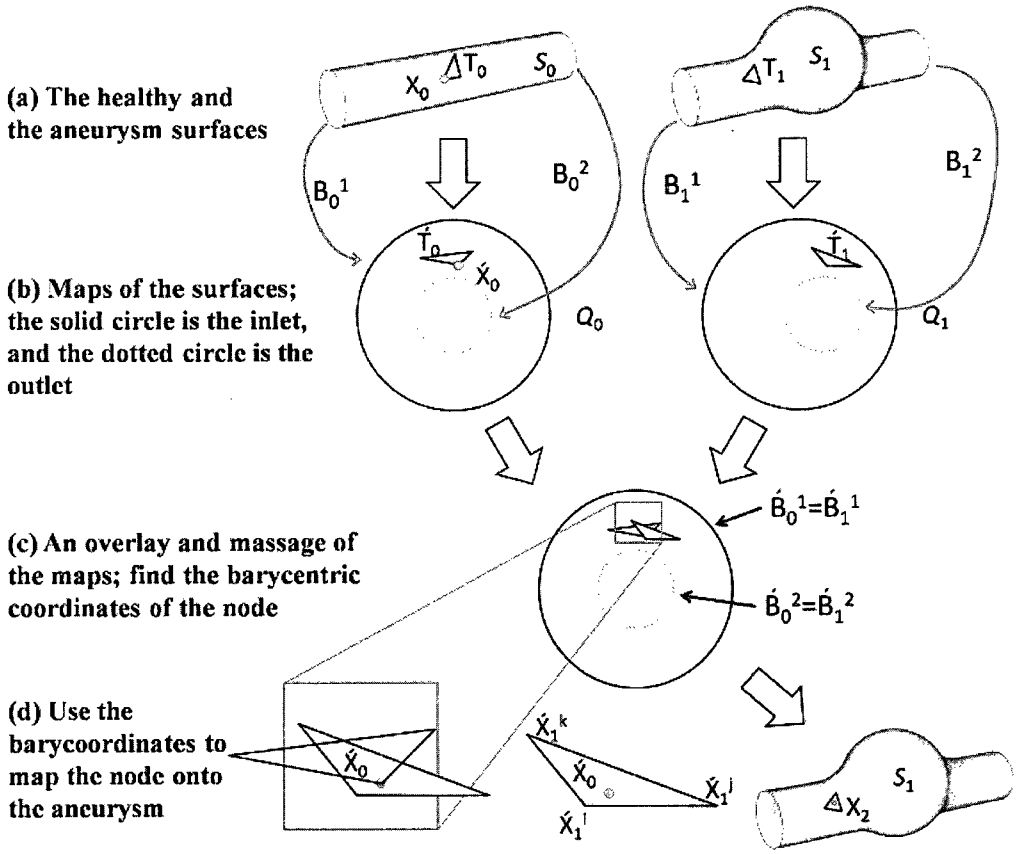

Figure 3-2: Mesh deformation following a node from the healthy surface (the red dot)

In order to create the mappings, the deforming (healthy) surface, S_0, and the desired (aneurysm) surface, S_1 , need to be triangulated into T_0 and T_1 respectively. While S_1 is generated from the aneurysm image data, a healthy model will need to be approximated if it does not already exist. For the patient-specific aneurysms presented in Chapter 5, the healthy

models are created manually within Autodesk® 3ds Max® by removing the aneurysm and smoothing the remaining surface. A uniform triangle-mesh is created with an advancing front method and is recommended to avoid weighting issues while relaxing the spring system later. In this algorithm, the inlet is the only opening left unmeshed. Every opening of the model is defined by a curve, and is called an end. Each end is B_s^e, where s is the surface ID ($s = 0$ represents the healthy model and $s = 1$ represents the aneurysm) and e is the number of the end, with $e = 0$ representing the inlet and $e = 1,2,\ldots$ the outlets. Note, all of the variables with an acute accent, `` ´ '', refer to their counterparts in the parametric space.

To ensure the domain of the mapQ_0s and Q_1 are identical, the nodes on the boundary of the disc are moved to a fixed radius, as shown in Figure 3-3. Thus the coordinates on the boundary of the disc are known, where $\acute{B}_0^0 = \acute{B}_1^0$, and as a result the location of the remaining nodes can be solved for. At this point the uniform parameterizations of S_0 and S_1 only have the same outer radius, see Figure 3-3(a). A uniform parameterization is chosen to map the surface-mesh onto a disc for simple implementation and computational efficiency. Since the method requires the mesh to be topologically equivalent to a disc, all but one inlet needs to be closed, leaving a single boundary. Since the concentration of nodes in each mesh is different, the radius and location of all the remaining ends in $Q_0$and Q_1 do not match, which is illustrated by the bifurcation in Figure 3-3(b). However, by moving an end and its pair toward the average of their centers, the validity of the mesh will be maintained while producing equivalent maps. The aligned ends can be seen in Figure 3-3(c) and allow the node in Figure 3-2(d) to map to the correct triangle in S_1 via barycentric coordinates. Contrary to our work in [111], it is much simpler and less time consuming to triangulate the outlets than it is to produce a parameterization for a disc with holes.

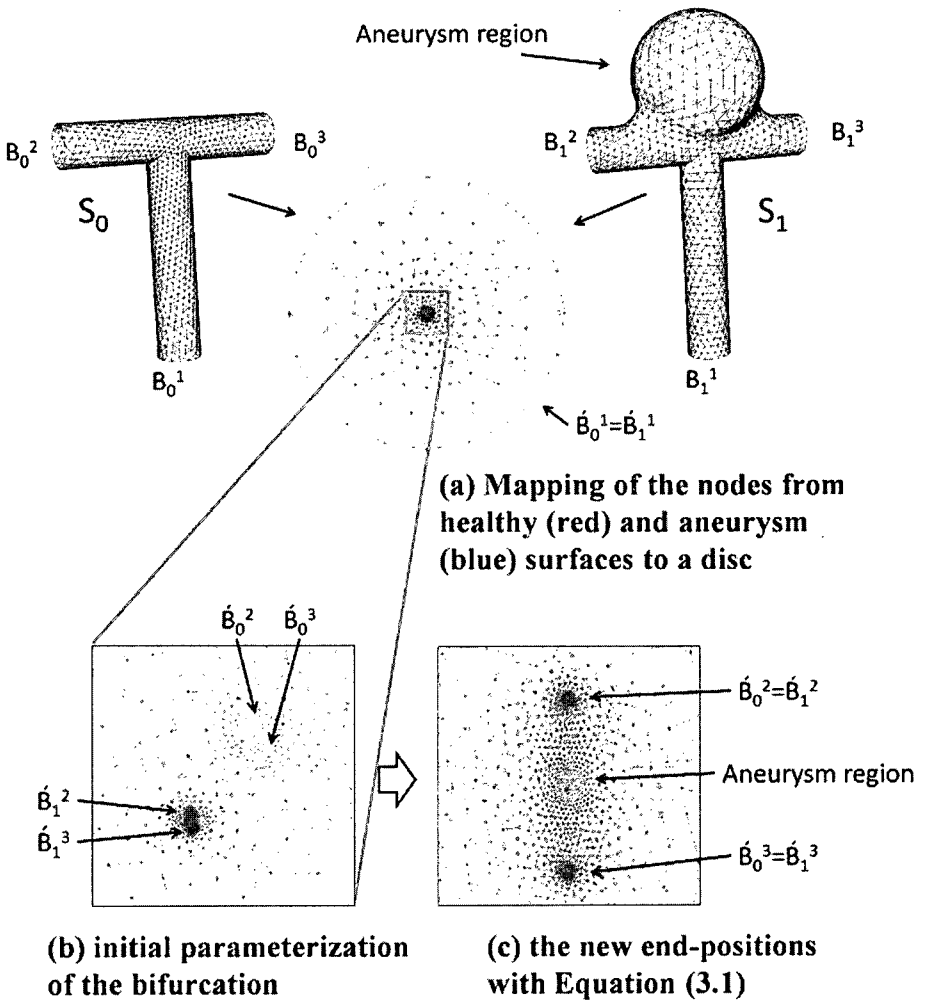

Figure 3-3: Aligning parameterizations from different surfaces

In order to ensure the meshes remain untangled when $\acute{B}_0^e = \acute{B}_1^e$, the nodes within a radius-of-influence (ROI) of each end should be moved according to Equation (3.1), where $\acute{\boldsymbol{x}}_i$ is the coordinate of a node in the map and $\acute{\boldsymbol{x}}_i'$ is its updated location, $\boldsymbol{p}_e$ is the vector from the end's current center to the average center of $\acute{B}_0^e$ and $\acute{B}_1^e$, r_i is the distance from the current node $\boldsymbol{x}_i$ to the center of the end being moved, and r_e is the radius of the end.

$$\acute{\boldsymbol{x}}_i' = \acute{\boldsymbol{x}}_i + \boldsymbol{p}_e \frac{k\|\boldsymbol{p}_e\| - r_i}{k\|\boldsymbol{p}_e\| - r_e} \tag{3.1}$$

The ROI size is determined by k and should be chosen between 1 and 100 to ensure enough of the mesh is smoothed while moving the ends. Here $k = 30$ is chosen, with larger values smoothing more of the mesh. With the only variable determining how far a node should move in each iteration being r_i, a linear decay within the ROI prevents element tangling. This moves the nodes of each end the largest distance, while those furthest from the center do not move at all. Additionally, the ROI naturally shrinks as the ends get closer to the final location because $\boldsymbol{p}_e$ becomes smaller after each iteration. Now that $\acute{B}_0^e = \acute{B}_1^e$, the radii of the ends can then be matched by shrinking the larger of the two. With equivalent maps, S_0 and S_1 cover the same parameterized domain and can be matched directly.

As shown in Figure 3-2, overlaying Q_0 and Q_1 provides any node from one map with a unique location in the other. The nodes in Q_0 are matched with coordinates from Q_1, which moves the mesh from S_0 onto S_1. If Q_1 is treated as a coordinate map, then every node in Q_1 takes its coordinates from S_1. With Equation (3.2), the corresponding node of $\boldsymbol{x}_0$ on S_1 is defined by the barycentric coordinates of $\acute{\boldsymbol{x}}_0$ within the triangle $\acute{T}_1$, where A, B, and C are the barycentric coordinates of $\acute{x}_0$ within $\acute{T}_1$ and $\boldsymbol{x}_1^i$, $\boldsymbol{x}_1^j$, and $\boldsymbol{x}_1^k$ are the three vertices of T_1 on S_1.

$$\boldsymbol{x}_2 = A\boldsymbol{x}_1^i + B\boldsymbol{x}_1^j + C\boldsymbol{x}_1^k \tag{3.2}$$

Each triangle is found by first locating the closest point in Q_1 to $\acute{\boldsymbol{x}}_0$ and then searching for the triangle, $\acute{T}_1$, that yields all positive barycentric coordinates.

The set of $\boldsymbol{x}_2$ definesS_2, which is mesh of the healthy vessel, after being deformed to match the *geometry* of the aneurysm, see Figure 3-1. However, S_2 does not take into account any stretching the vessel undergoes. In order to incorporate the elastic, stretching nature of the vessel tissue, the Fung material model [43] will be used in the next section when relaxing the mesh using springs.

3.2 Spring Relaxation to Smooth the Surface Mesh

While the geometry has been matched, the mesh of S_2 can better approximate the deformation if it is treated as a spring system. Changing all the edges into springs, connected at the nodes, the system will relax into a more natural state. This will primarily stretch the elements around the aneurysm region, producing a final configuration that mimics the stretching of the vessel wall. The nodes are iteratively moved through two force-equilibrium equations until a threshold is met.

For both equilibrium sets, the new location of $\boldsymbol{x}_2$, $\boldsymbol{x}_2'$, is given by Equation (3.3), such that K is the average stiffness, $\boldsymbol{F}$ is the total force acting on the node, and s is 10% of the minimum length of the connected springs, which prevents nodes from taking too large a step and tangling.

$$x_2' = x_2 + s\frac{F}{K} \tag{3.3}$$

Throughout the process, the nodes are projected onto the closest point oS_1f to ensure S_2 does not deviate from the desired shape. The final, deformed blood vessel, S_3, has the shape of the aneurysm and takes the elasticity of the tissue into account, refer back to Figure 3-1.

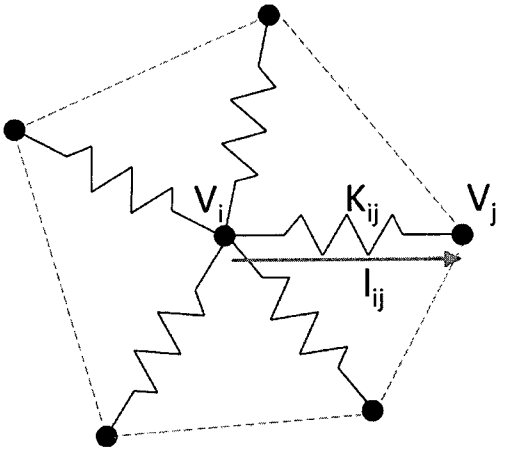

Figure 3-4: Spring model of nodal-neighborhood for the point of interest

3.2.1 Initial Laplacian Smoothing

The first set of iterations uses Laplacian smoothing to provide an initial guess at the elasticity in the vessel. Laplacian smoothing moves a node to the geometric center of its neighbors. If a node is connected to a series of zero-length springs, Laplacian smoothing is equivalent to finding the location of the node where the forces are balanced. As such, the direction a node needs to be moved and the direction of the force acting on it are the same and can be found through Equation (3.4), where F_i is the force acting on node x_2^i, $K_{ij} = 1$ is the stiffness of

the spring between vertices x_2^i and x_2^j, $\boldsymbol{l}_{ij} = \boldsymbol{x}_2^j - \boldsymbol{x}_2^i$, and N_i is the neighborhood of x_2^i. Figure 3-4 shows the neighborhood of a single node.

$$\boldsymbol{F}_i = \sum_{j \epsilon N_i} K_{ij} \boldsymbol{l}_{ij} \tag{3.4}$$

Iterations are terminated when every node has moved less than 5% of the local, minimum edge-length. A queue is created containing every node of the mesh, which are then individually removed as each falls below the termination criteria. By not requiring nodes to move that do not have to, the size of the list is reduced and method significantly increases the speed of the algorithm. However, if a node moves by more than 2.5% all of its neighbors are reintroduced to the list. This allows a neighboring node to move that may have been restrained before. While this step terminates quickly, it is capable of moving the nodes out of positions that could tangle were finite-length springs used and provides an initial guess at the elasticity in the vessel.

3.2.2 Linear versus Non-Linear Elasticity

The second set of iterations use springs with a finite length to incorporate whether the tissue is in compression or tension. Because the mesh started on the healthy model with edges of a known size, any positive or negative growth, due to the deformation, is going to influence how an edge responds. Using zero-length springs improved the starting location for the spring relaxation, but were insufficient at providing a physically meaningful solution. Equation (3.4) can be modified to Equation (3.5) by using the original edge lengths from S_0,

where $\hat{\boldsymbol{l}}_{ij}$ is the normalized vector from $\boldsymbol{x}_2^i$ to $\boldsymbol{x}_2^j$, and $\|\boldsymbol{x}_0^j - \boldsymbol{x}_0^i\|$ is the original length of the spring.

$$\boldsymbol{F}_i = \sum_{j \epsilon N_i} K_{ij}\left(\boldsymbol{l}_{ij} - \|\boldsymbol{x}_0^j - \boldsymbol{x}_0^i\|\hat{\boldsymbol{l}}_{ij}\right) \tag{3.5}$$

Through Equation (3.5) a node moves according to the tensile and compressive forces acting upon it and not just to the center of its neighbors.

Terminating this set of iterations is accomplished when the motion of every node is less than 0.05% of the local, minimum edge-length. There are two reasons for stricter requirements on the termination criteria. First, the motion of any node in this step is likely to be smaller. Second, the mesh resulting from this step will be used to calculate the wall thickness, while the Laplacian smoothing was used to provide a *good-enough* starting position. Increased iterations area necessary to ensure nodes settle into their final location.

As discussed in Chapter 2 the vessel wall is a non-linear material. That is, as the strain is increased the tissue becomes stiffer. A linear-elastic material, on the other hand, remains unvarying in its stiffness regardless of how much it is stretched, and is realized when K_{ij} is constant. The question is then raised as to if and how the material properties of blood-vessel tissue should be included. As described in [78], the use of either linear or non-linear material models during simulations exhibit the same trend in stress distribution, with extrema occurring at the same locations. Since stress is directly related to material thickness, if the change in wall thickness is negligible between the two models, there is little reason to include a more intensive calculation.

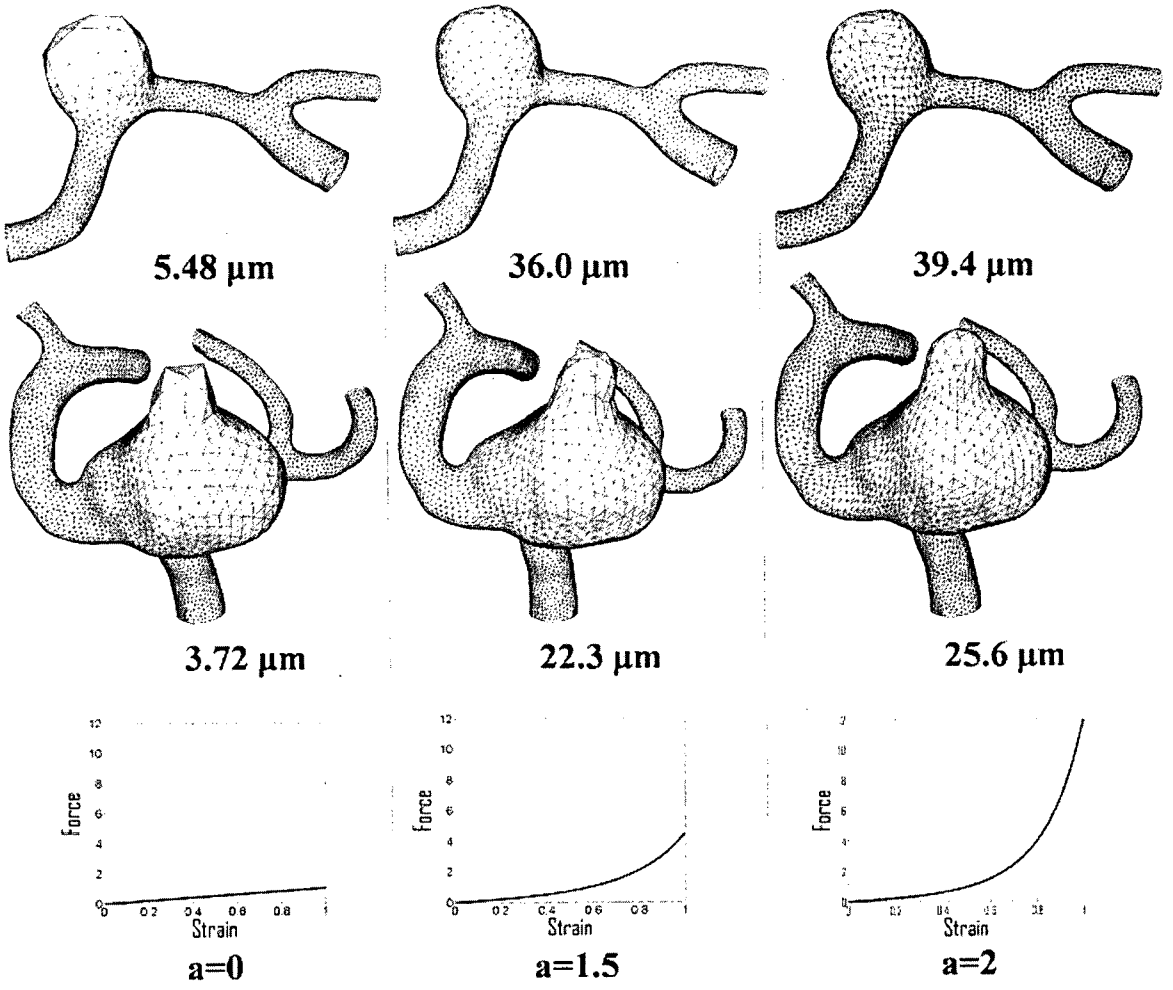

Figure 3-5: Deformed mesh by given non-linear springs, with minimum thickness

The strain-energy function for blood-vessel tissue developed by Fung [43], Equation (2.1), can be simplified as an isotropic material in Equation (3.6).

$$K_{ij} = Ce^{a\varepsilon_{ij}^2} \tag{3.6}$$

The result is an isotropic, strain-strengthening model for finite-length springs, where $C = 0.002$ and $a = 1.5$ are constants used to approximate the stress-strain curve for vessel tissue, while yielding a range of thickness values that match the medical data, and ε_{ij} is the strain of the spring. The distribution is most affected by changing a, where setting $a = 0$ returns Equation (3.6) to a linear, finite-length spring and an increase in the coefficient will make the springs stiffer. The latter will result in a larger minimum-thickness as the springs are less able to stretch. The advantage of using Equation (3.6) is that the material directions do not need to be determined; whereas, making use of the anisotropy in Equation (2.1) does require them.

Using this model, though not anisotropic like the true vessel material, provides a more accurate guess at the stretching of the surface than a linear model could. As can be seen in Figure 3-5, changing the constants in Equation (3.6) can give a substantially different distribution of the mesh, and as a result substantially increases the minimum wall-thickness. Comparing the meshes from the linear and non-linear models, there is an upwards of 600% increase in the minimum element size. Using a non-linear model produces a significantly different mesh and proves it is necessary to providing a more accurate approximation of the stretching vessel surface. Increasing both a and/or C will make the material stiffer for a given strain and the constants should be chosen based on medical data in order to represent the real material nature.

3.2.3 Isotropy versus Anisotropy

In addition to blood-vessel tissue being non-linear, it is also anisotropic and may need to be included in the mesh deformation. Though, as with the non-linearity, adding anisotropy to the algorithm needs to produce a beneficial change. That is, the stress-strain relationship

should be significantly larger in one direction than the other. And in particular, the tissue should act anisotropically over the range of strains during the growth of an aneurysm.

A closer inspection of Equation (2.1) shows there is the potential for a significant divergence if the coefficients for the axial and circumferential strains are different enough. Shown in Figure 3-6 is a plot of the decoupled strain-energy curves. As can be seen, the circumferential strain is substantially stiffer than its counterpart. This means blood-vessel tissue should display a large change in behavior depending on how it is stretched.

The primary difficulty in adding anisotropy to an arbitrary aneurysm model is the difficulty in determining the material directions. And as described in Chapter 2, the simulations that do contain anisotropy uses the spine of the model, which does not provide sufficient information for aneurysms with complex shapes. While the material directions may appear obvious to an observer, it is not intuitive for a computer and makes automation difficult. Additionally, the deformation of the material has the potential to no longer be aligned with the axis and circumference of the aneurysm.

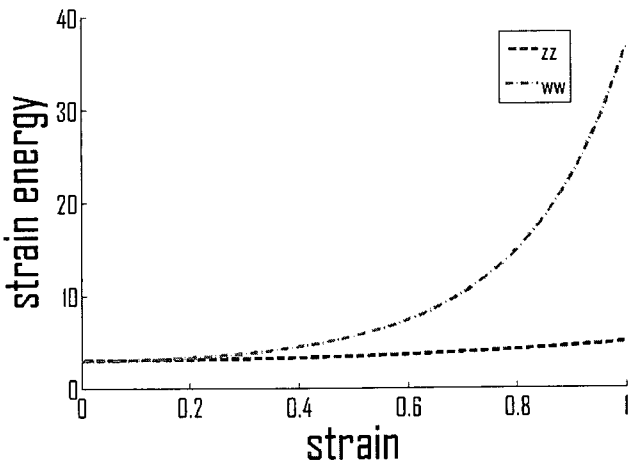

Figure 3-6: Strain-energy curve for anisotropic tissue

A more detailed description of how an anisotropic material model can be added to the algorithm is presented in Chapter 6. Like with the wall thickness, the original material directions can be calculated from the principle-curvatures of the healthy model and passed through the mesh deformation onto the aneurysm. By using the new directions, the spring system can be relaxed anisotropically in the same manner as Section 3.2.

3.3 Calculating Equivalent Wall Thickness

The initial thickness, T_0, of a healthy cerebral artery wall is 15-20% of the vessel radius. Instead of using a constant value over the entire domain, the Laplace equation is solved across S_0, with only the thickness at the ends being defined [6]. This provides a smooth wall-thickness throughout the volume; however, unlike [6] these values are only used for the healthy model and provide a *better* starting condition than using a uniform thickness.

The wall thickness at every node in S_3 can now be calculated. The deformed and relaxed mesh has elements of different size than originally, and the area change between T_0 and T_3 can be compared directly. During the initial aneurysm growth, the volume of the tissue is assumed to be conserved since the Poisson's ratio of tissue is a constant, the deformation is elastic, and little collagen mass is added. As a result, the change in wall thickness is inversely proportional to the change in the element area. At every node x_3, the wall thickness, t_3, is related to the average ratio of the area change of the neighboring triangles, and can be found through Equation (3.7), where A_0^j and A_3^j are the areas of triangles T_0 and T_3 respectively, and N is the valence number of x_3^i.

$$t_3 = t_0 \frac{\sum_{j \epsilon N_i} \frac{A_0^j}{A_3^j}}{N} \tag{3.7}$$

Geometry and a prismatic mesh for the blood vessel wall could be created directly from this information. However, S_1 provides a higher quality surface-mesh than S_3 because it was never stretched. As a result, all the wall-thickness information is mapped from the deformed mesh, S_3, back to the original aneurysm model, S_1, by using the barycentric coordinates of x_1 within T_3. Figure 3-1 shows the final wall thickness and wedge/tetrahedral mesh of the fluid region; the latter is discussed in Chapter 4. As can be seen in the figure, there is the potential for significant change in the wall thickness over a small distance.

Equation (3.7) assumes no mass is added to the vessel wall during its initial growth; however, the amount of collagen will increase over time. An alternative equation, where approximations of this growth are incorporated, is given by Equation (3.8), where D is the percent increase in volume and λ is the area stretching ratio. This formulation can be modified as more information becomes available about the rate of collagen growth and what causes it.

$$t_3 = t_0 \frac{\sum_{j \epsilon N_i} \frac{A_0^j}{A_3^j} \left[1 + \frac{D}{\lambda - 1}\left(\frac{A_3^j}{A_0^j} - 1\right)\right]}{N} \tag{3.8}$$

Equation (3.8) adds a linearly increasing amount of collagen in regions of high strain. The wall-thickness increases with a rise in D, as can be seen in Figure 3-8. When $D = 0$, Equation (3.8) becomes Equation (3.7). Further modifying a and C in Equation (3.6) will

affect the global distribution of the vessel mass, while changing D will alter the minimum thickness through mass addition, as seen in the plot of Figure 3-7. As better distributions become available, Equation (3.8) can approximate the wall-thickness more accurately.

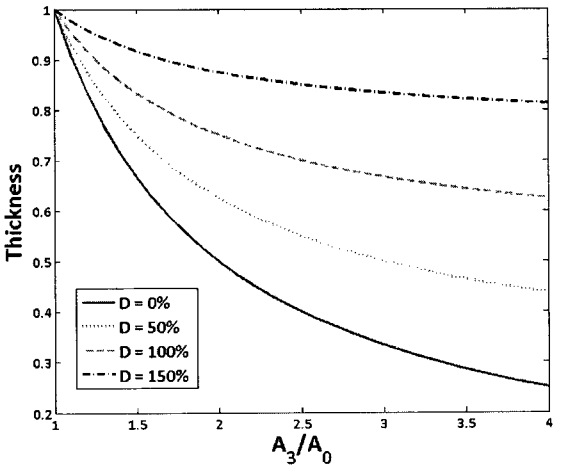

Figure 3-7: Plot of increasing thickness at fundus for increasing D.

3.4 Mesh Coarseness Independence

A concern with this algorithm is whether the wall-thickness estimation results are sensitive to the input mesh. A mesh that is too coarse may not represent the domain adequately, and too fine a mesh is computationally expensive. Fortunately, the mesh resolution does not seem to be an important factor in determining the wall-thickness of the aneurysm. Figure 3-8(a) shows the coarsest mesh used to determine the thickness sensitivity as well as the location of the sample points on S_1. As can be seen in Figure 3-8(c), the thickness is almost the same at every sample point in Figure 3-8(b) regardless of the number of nodes in the surface mesh. This means the results are not sensitive to the number of elements in the surface-mesh. A finer mesh will match the geometry more closely, but the trends in the thickness are independent.

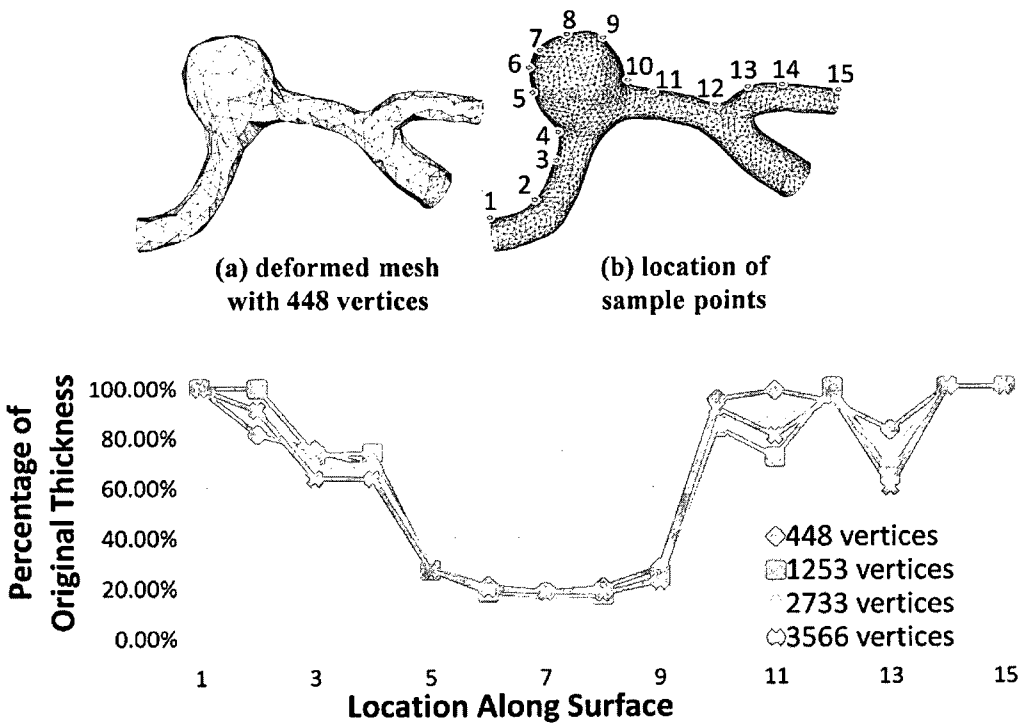

Figure 3-8: Plot of mesh independence and location of sample points

Related to this is the quality of the accuracy of the healthy model to the *true* starting geometry. The final model will vary slightly depending on the method used, e.g. by hand, an automated algorithm with curvature smoothing, etc. However, this will not produce any significant variation on the final wall thickness because the scale of the variances in the healthy models is order of magnitudes smaller than the deformation it undergoes.

3.5 Summary

This chapter presented the principle method for improving simulations of patient-specific aneurysms. Through the deformation of a single mesh, the aneurysm wall-thickness

can be found and is independent of the mesh used. Surface parameterization is used to map the mesh of one model onto the other, and spring-relaxation provides a means to manipulate the mesh in a physically meaningful way. With the addition of a non-linear, anisotropic models, the final deformation provides insight into how the blood vessel deformed and a model that can be used for simulations. The effect of using a model with a variable wall thickness is demonstrated through the FSI analyses in Chapter 5.

Chapter 4

Boundary-Layer Meshing

A mesh of the fluid domain is required before a CFD or FSI simulation can be run. As with meshes for structural domains, the type and quality of the mesh plays a factor in the results produced by the solver. For fluid domains this means elements should be aligned with the flow, and if the flow is influenced by any walls, a mesh that properly resolves the boundary-layer region is essential.

While advancing front methods (AFMs) are commonly used to mesh a domain, they are almost exclusively concerned with generating tetrahedral meshes. The algorithms that do use prismatic elements have problems with overlapping of fronts and will often remove elements from layers, or entire layers from the mesh. This complicates the mesh by requiring additional elements and limits the ability of a boundary-layer mesh to capture flow phenomenon. However, the benefit of using prismatic elements is that in addition to being boundary-aligned, they can reduce the computational cost associated with solving the simulation.

This chapter presents a tool to prevent the collision of boundary-layer mesh fronts with a medial-ball based sizing function. By using the sizing function, AFMs will be better able to fill a boundary-layer region with prismatic elements. The resulting mesh is usable in CFD and FSI solvers.

4.1 The Initial Mesh and Hairs

A hair is a vector anchored at each node of a surface mesh and is used to guide the creation of the prism-layers. The direction and length of a hair is determined by the local surface mesh, with subsequent smoothing and trimming used to improve the overall quality of the final elements.

Hairs are constructed on a surface mesh, which can be generated by any method, e.g. paving [112]. Pointing into the volume, the initial length of a hair is chosen to produce isotropic elements in the interior-most layer of the boundary-layer mesh, with the starting direction normal to the surface. Hairs at corners take the average direction of their neighbors. Limiting the mesh to one hair at each node guarantees the entire boundary-layer mesh is composed of prismatic elements; however, if this were not a constraint, additional hairs could be added. In order to reduce the computational cost of optimization performed for every layer, the length of each hair is the total thickness of the boundary-layer mesh, and the individual layers are subdivided out at the end.

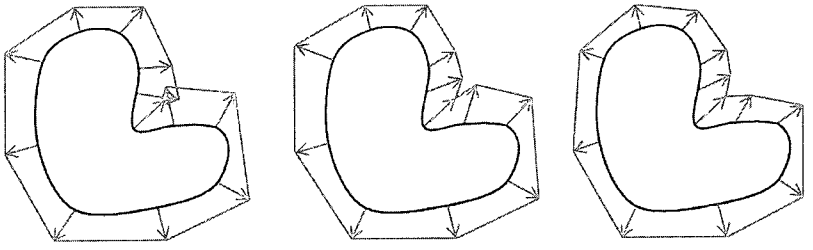

Figure 4-1: Improvements to boundary-layer mesh from sizing function and smoothing

A medial-ball based sizing function [20,21,113], which calculates the radius of the largest sphere that can fit between two or more surfaces throughout the volume, is used to prevent the fronts from colliding. The radii of the spheres are compared against the boundary-layer mesh thickness to determine if a hair needs to shrink. While the sizing function will eliminate front collisions, smoothing the hairs further accomplishes three things: (1) pushes the growth of the elements away from tight corners, (2) prevents "tucking", and (3) provides a smoother transition between hairs of varying length. The benefits of smoothing can be seen in Fig 4-1.

4.2 Medial-Ball Based Sizing Function

Thin regions of the geometry may prove to be too narrow for a boundary-layer mesh that uses the initial thickness. However, instead of removing layers from the mesh, hairs are shortened in order to prevent the mesh fronts from overlapping. Since the length of a hair is the total thickness of the boundary-layer mesh, reducing this value binds all the mesh elements to the foreshortened region. Using the medial-ball based sizing function presented by Quadros [20,21], if the length of a hair is longer than the local radius, it is shortened, which ensures that no fronts overlap.

A point-region (PR) octree is created as a background mesh and balanced so there is at most one level of growth between the cells. The PR-octree was chosen because it is able to capture small features and high curvature regions of the domain while creating a grid that is order independent. The PR-octree starts larger than the domain's bounding box and is oriented with the Cartesian coordinates. The cells are subdivided until the maximum, user-defined, depth is achieved or until each cell only contains one or no vertices. Setting a maximum depth prevents excessive refinement of small features, which increases the speed

of the algorithm and conserves memory. All the nodes of the background mesh are labeled as either interior or exterior to the domain and the final grid is pruned to just the cells that are interior to and on the boundary of the domain.

Using a grassfire approach, the medial-ball is found when fronts from competing surfaces meet. The background mesh stores the radius of the medial-ball and uses a quadratic, inverse-distance weighted interpolation to fill the remaining space. Starting from the outermost nodes interior to the domain, the grassfire is propagated inward to nodes that have not been visited. Newly visited nodes are added to a priority queue based on the shortest distance to the boundary. The node that is closest to the surface is popped and any unvisited neighbors are added to the queue. This terminates when all the interior nodes of the PR-octree have been visited and the locations where the fronts meet were marked. The marked nodes provide the skeleton for the domain and the locations where the radii are stored.

By using a medial ball, the skeleton will capture thin geometry and corners; however, acute corners can cause singularities in the sizing function. As adjacent surfaces come together, the radius of the largest sphere that fits between them will tend toward zero. Since most corners will not cause fronts to overlap, the skeleton is trimmed at all the corners larger than 45°. Keeping the skeleton in these small corners ensures the boundary-layer mesh shrinks only in corners where collisions may likely occur.

Calculations for the radii stored on the skeleton are split into three cases where: (1) no grid points exist between the surfaces, (2) one grid point is in between, and (3) multiple grid points are between the surfaces, as shown in Figure 4-2(a),(b), and (c) respectively. The grid point where the grassfire fronts meet in Case 2 is $\boldsymbol{q}$, while the adjacent points to the front

collision are $\boldsymbol{q_1}$ and $\boldsymbol{q_2}$. In order to calculate the radius of the medial ball, a reference location on the surfaces needs to be picked. While the octree was subdivided to capture the volume, the grid points will likely not lie on any surfaces. Therefore, the intersection of the edges between the interior and exterior octree points and the surfaces of the domain will be used. For case 2 the radius is defined by Equation (4.1), where d_1 and d_2 are the distances from $\boldsymbol{q}$ and the nearest surfaces, calculated using the normals, $\boldsymbol{n_1}$ and $\boldsymbol{n_2}$, for the closest pair of surfaces.

$$r = \frac{d_1 + d_2}{2} \tag{4.1}$$

Case 1 is a variation of case 2 where $\boldsymbol{q}$ is the midpoint between the intersection points. The radius for case 3 is found Equation (4.2), where d is the distance between $\boldsymbol{q_1}$ and $\boldsymbol{q_2}$.

$$r = \frac{d_1 + d_2 + d}{2} \tag{4.2}$$

Preventing the fronts from overlapping requires that the length of every hair is smaller than the radius on the background mesh. When the length of a hair is checked against the closest octree value, the hair will take the shorter of the two. A user-defined coefficient between zero and one, for this paper $c = 0.75$, is multiplied in to ensure there is space between the fronts. By providing space between the fronts for additional mesh elements, this eliminates the need for the prismatic elements from opposing fronts to be aligned. The

resulting boundary-layer mesh has no overlapping fronts and is only shortened near the thinnest regions of the geometry.

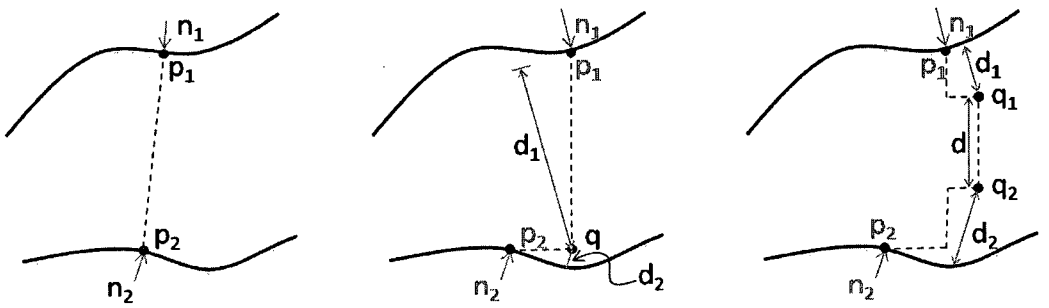

(a) Case 1 **(b) Case 2** **(c) Case 3**

Figure 4-2: Calculation of medial-ball radius

4.3 Smoothing

While no front-collisions exist, smoothing the direction and length of each hair will improve the mesh quality.

4.3.1 Smoothing Directions

Hairs near an edge or vertex may point in significantly different directions, and plays as much of a factor in tangling elements as the length of the hair does. To provide a transition between the hairs on the boundary and those on the interior of a surface, every hair takes the average of its neighbors. Three iterations are performed over every hair. Occasionally a hair may have an orientation that is substantially different than the average. In this case the hair moves toward the average direction through Equation (4.3), where $\boldsymbol{h}$ is the hair at the current node and $\widehat{\boldsymbol{h}}$ is its regularized form, $\boldsymbol{h}'$ is the newly modified hair, and $\boldsymbol{v}_j$ is the direction of each of the N neighboring hairs.

$$\boldsymbol{h'} = 0.9\widehat{\boldsymbol{h}} + 0.1\left(\sum_{j=1}^{N} \frac{\boldsymbol{v_j}}{\|\boldsymbol{v_j}\|} - \widehat{\boldsymbol{h}}\right) \tag{4.3}$$

This allows the neighbors of the hair to shift toward the final orientation instead of forcing the average direction. While smoothing the directions will not affect a majority of the hairs, it will point them out of acute corners.

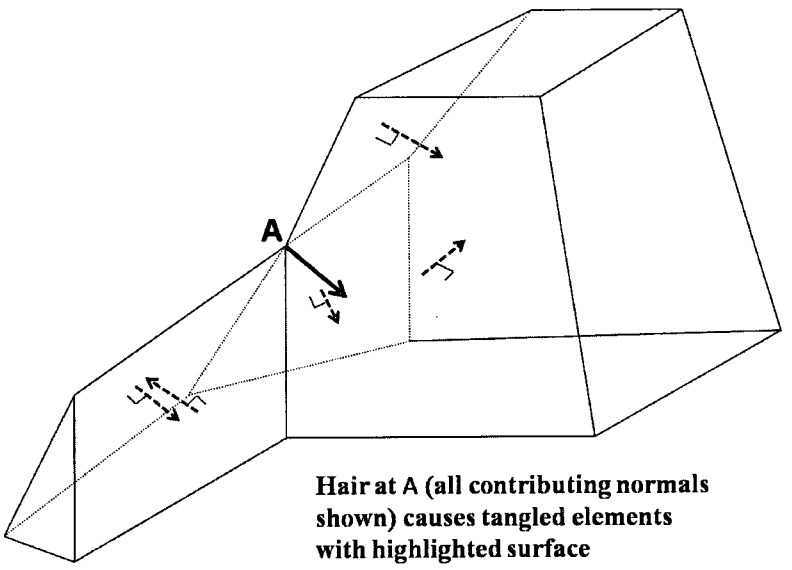

Figure 4-3: Invalid hair direction due to overweighting by neighbors

Though not common, there is a chance the initial direction of a hair will point outside of the domain. This occurs at corners where multiple faces point in a similar direction and *push* the average outside. To correct this, the tip of the hair tries to move to a location where it can be seen by the adjacent surfaces. This means that the hair has a positive dot product with all of its neighbors and the location can be optimized through Equation (4.4).

$$\max \min_{j=1:N} \hat{\boldsymbol{h}} \cdot \frac{\boldsymbol{v}_j}{\|\boldsymbol{v}_j\|} \tag{4.4}$$

A negative dot product would cause elements to form outside the domain. As such, an approximation of the optimization problem is achieved by marching a hair in the direction of the neighbor that produces the smallest dot product. The direction changes when the dot product with another neighbor is smaller. Marching is continued until any additional movement starts to minimize the value.

4.3.2 Smoothing Lengths

There are two instances where the length of a hair needs to be refined. The first case is *tucked* corners, and is a direct consequence of the geometry. Tucked corners are where hairs, at vertices and along edges, are recessed relative to their neighbors, with an example being shown in Figure 4-1(b). The second case is the more general and occurs when an individual hair has a length that is different length than its neighbors.

Given that a hair at a corner takes the average direction of adjacent surfaces, it will always appear shorter than if it were perpendicular to a single surface. This leads to any elements created becoming increasingly skewed at sharper corners. By lengthening these hairs the boundary-layer mesh will better reflect the surface geometry and contain higher quality elements. This can be accomplished by lengthening hairs in these locations by a factor, g, based on the angle off the surface, α_j. A hair can be given a new length, as defined by Equations (4.5) and (4.6), where the value of g is a measure of α_j between 0° - 180°, and $\boldsymbol{d}_j$ is the vector pointing from the base of the hair to one of its neighbors.

$$\boldsymbol{h'} = \frac{\boldsymbol{h}}{1 - |1 - g|} \tag{4.5}$$

$$g = \frac{1}{N}\sum_{j=1}^{N} \begin{cases} \left\| \frac{\boldsymbol{d_j}}{\|\boldsymbol{d_j}\|} \times \widehat{\boldsymbol{h}} \right\| & if \ \propto_j \leq 90° \\ 2 - \left\| \frac{\boldsymbol{d_j}}{\|\boldsymbol{d_j}\|} \times \widehat{\boldsymbol{h}} \right\| & else \end{cases} \tag{4.6}$$

A concern with lengthening any hair is the possibility of tangling elements. By ensuring a hair remains shorter than any adjacent edge, $\boldsymbol{h} \cdot \frac{\boldsymbol{d_j}}{\|\boldsymbol{d_j}\|} < \|\boldsymbol{d_j}\|$, a hair will not intersect any of its neighbors. In the case where a hair does need to be shortened, the neighbors are shortened as well to reduce the element skew.

For the remainder of the hairs a few iterations of Laplacian smoothing will remove any large differences in their lengths. However, the values measured should be the length of a hair's neighbors projected against itself through Equation (4.7).

$$\boldsymbol{h'} = \frac{\|\boldsymbol{h}\| + \sum_{j=1}^{N} \boldsymbol{v_j} \cdot \widehat{\boldsymbol{h}}}{N + 1} \widehat{\boldsymbol{h}} \tag{4.7}$$

This is the same as averaging the shortest distance from the tips of the hairs to the surface, but removes any ambiguity over which surface hairs at corners should be measured against.

4.4 Finishing Mesh

The boundary-layer mesh is generated once all the hairs have been smoothed and adjusted to ensure no fronts will overlap. Using the hairs, the surface mesh is extruded and subsequently subdivided into the desired number of layers. Applying a gradient to the growth of the layers allows highly anisotropic elements along the surface while transitioning to isotropic elements in the outermost layer. For this paper the remainder of the domain is filled with tetrahedra. When using hexahedra in the boundary-layer mesh, the exposed quadrilateral faces are joined to two tetrahedra. This non-conforming mesh is usable in finite-volume solvers. Further smoothing could be performed, to further increase the element quality, as a post process to finishing the mesh, but falls outside the scope of this paper.

4.5 Examples

This chapter presents four models to show the advantage of using a sizing function based on the medial-ball. This was implemented in CUBIT [114], with a default of 15 layers and a gradient of 1.2 for the growth of the boundary-layer mesh. The mesh data for each of the models can be found in Table 4-1. In all the cases, the domains exhibit features which would cause the boundary-layer mesh to overlap and tangle. The proposed method is able to capture these small regions without removing any elements from the mesh layers. This not only keeps the desired number of elements in a thin region, but it also allows prismatic elements to be used in more CFD boundary-layer meshes.

The first mesh is generated around an extruded three-piece airfoil. Creating a boundary-layer mesh by only specifying the number of layers and rate of growth can produce the results seen in Fig 4-4(a). As such, the three-piece airfoil has three, highlighted

regions where overlapping occurs; both from competing fronts and from tangling in a high-curvature region. By limiting the growth of the boundary-layer mesh in the thin regions, a mesh suitable for simulations can be created in an automatic manner and maintain the desired number of layers and their rate of growth. The final boundary-layer mesh for the three-piece airfoil, seen in Figure 4-4(b), has 356820 hexahedra. A three-dimensional simulation at Mach 0.3 was run on the mesh in Figure 4-5 using ANSYS®, CFX™, giving the pressure profile seen in Figure 4-6. With a total of 986033 elements, and using the steady state transport model, a maximum pressure of 6102 Pa was found.

Table 4-1: Boundary-layer mesh statistics for four domains

		Aspect Ratio		Scaled Jacobian	
Model	# elements	minimum	maximum	minimum	average
Airfoil	356820	1.0	2132	0.26	0.95
Missile	239910	1.0	27160	0.20	0.84
Chamber	71910	1.8	1570	0.23	0.90
Aneurysm	70620	2.7	535.5	0.21	0.83

elements (hexahedra in all but the aneurysm, which is comprised of wedges) in the boundary-layer mesh

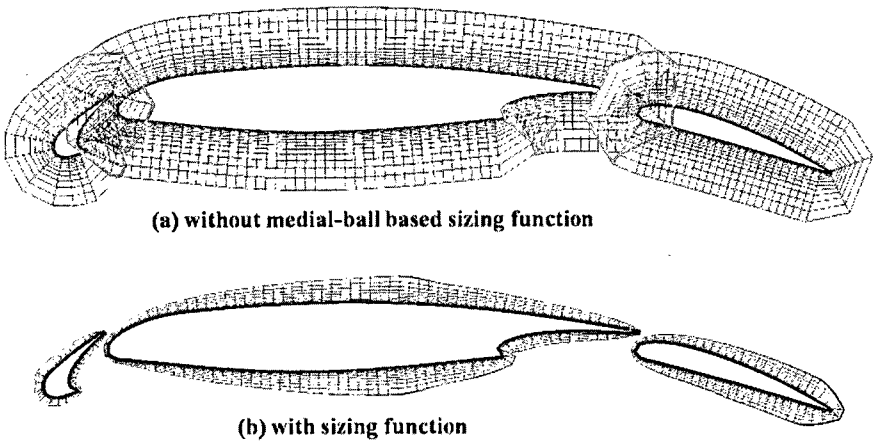

Figure 4-4: Boundary-layer mesh for three-piece airfoil

While the mesh of the surfaces for the combustion chamber, seen in Fig 4-7, and the missile, Fig 4-8, may not be ideal for simulations, the various element sizes demonstrate the ability of the sizing function to adjust the boundary-layer mesh to accommodate the thin region. Both domains have features that are significantly smaller than the average element length, but the mesh is able to maintain a scaled Jacobian above 0.2 without any post-processing.

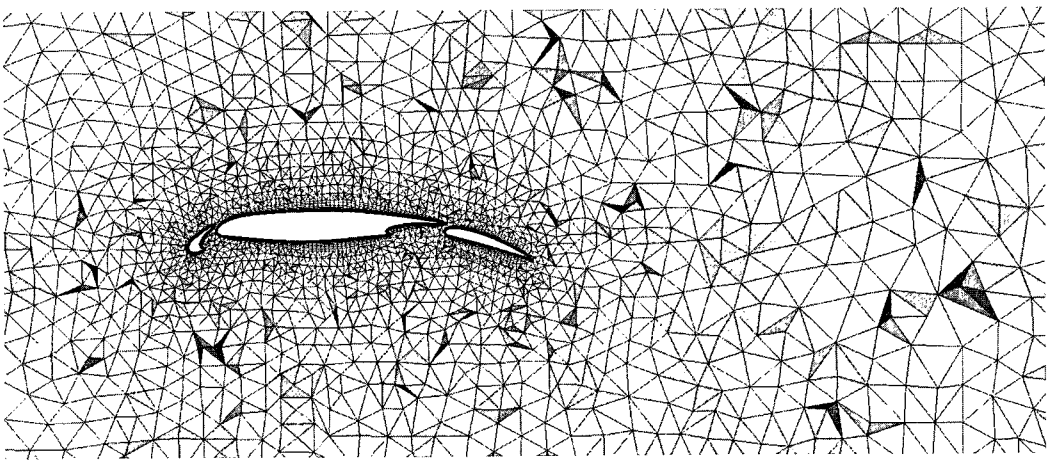

Figure 4-5: Full, hybrid mesh of three-piece airfoil used for CFD simulation

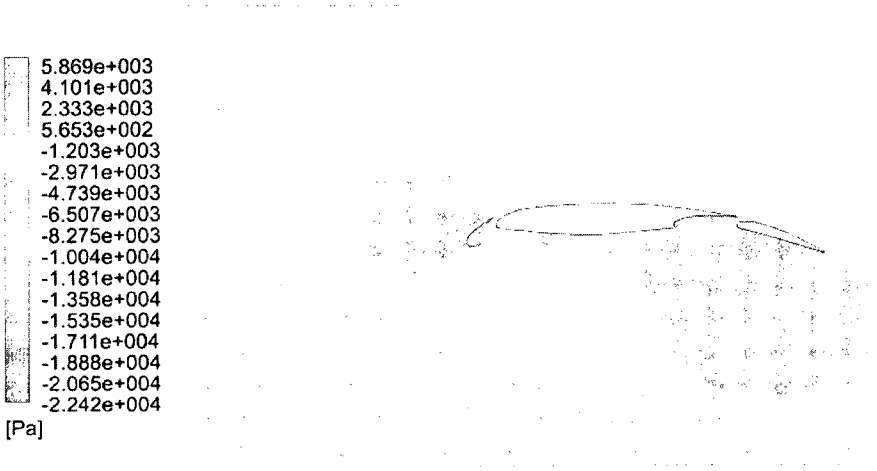

Figure 4-6: Pressure plot of three-piece airfoil at Mach 0.3

The final model is an example of aneurysm with multiple, shrinking branches, and can be seen in Fig 4-9. As the blood vessel splits, the boundary-layer mesh needs to shrink in order to fit within the narrowing passages. Without a sizing function that captures the local radius, the size of the boundary-layer mesh would cause overlapping in the smallest vessels.

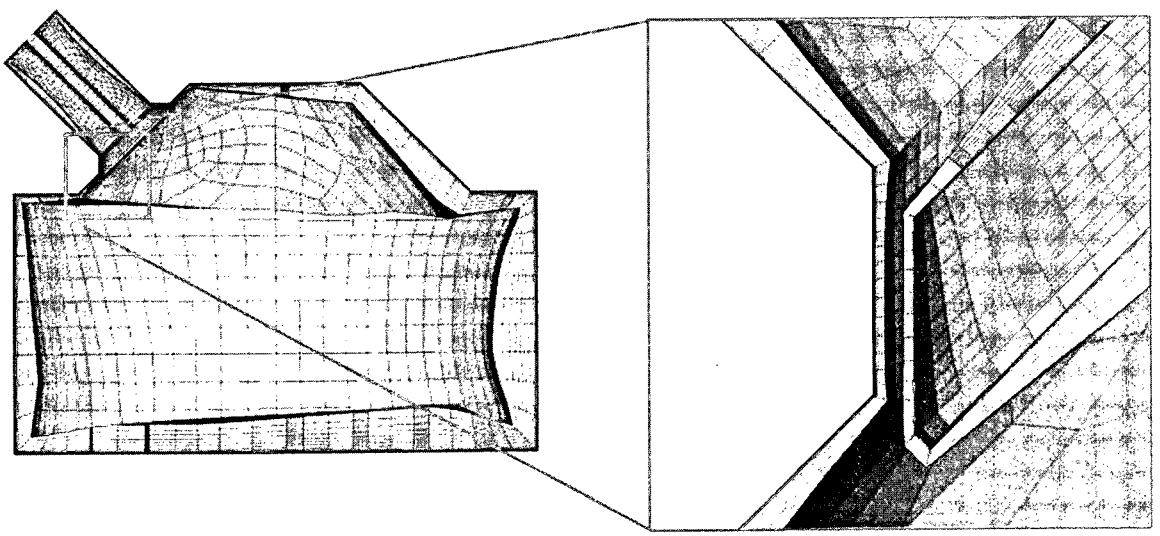

Figure 4-7: Boundary-layer mesh of combustion chamber with zoom

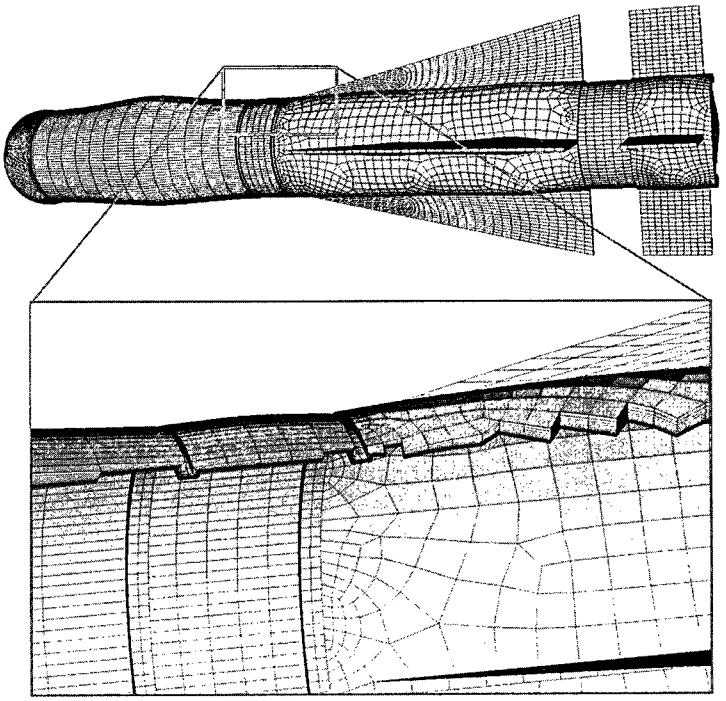

Figure 4-8: Boundary-layer mesh for missile with zoom

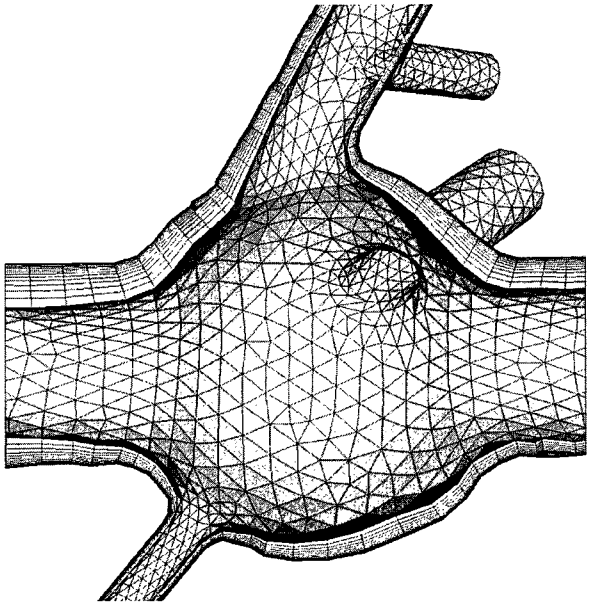

Figure 4-9: Boundary-layer mesh of aneurysm

4.6 Summary

This chapter presented a tool to prevent the boundary-layer mesh from overlapping while using an advancing front method. With this, a prismatic boundary-layer mesh can be created. Through the use of a medial-ball based sizing function the growth of the mesh can be reduced in local areas that are likely to collide. Additional smoothing is used to improve the element quality and minimize any additional tangling. The proposed method can generate high quality meshes over domains with various feature sizes that can then be used to perform computational fluid dynamic simulations.

Chapter 5

Thickness and Simulation Results for Aneurysms

In this thesis, four models were created and meshed with the presented methods and then simulated to find the maximum wall stress at peak systole in order to compare the results between the current aneurysm models and those with our equivalent wall thickness. FSI simulations were performed on all the models with a weak-coupling between ANSYS® v12.0 and ANSYS®, CFX™ v12.0. A converged solution for the interface displacement is found by iterating between the fluid and solid solvers during each timestep. The base model is a simplified aneurysm with one inlet and one outlet, which has previously been used to approximate abdominal aortic aneurysms (AAAs), was compared against the results simulated by Scotti [73] and used to validate the presented method. The remaining three models are patient-specific cerebral aneurysms, with the healthy models created from them by hand. Two of the cerebral aneurysm models are compared against results found in [6].

The mesh of the aneurysm walls is an extrusion of the surface mesh and subdivided into two layers of wedges. Several boundary layers were generated in the fluid-volume, which plays a particularly important role in the development of the flow and the resultant wall stresses. The fluid-volume mesh was created using the advancing-front method presented in Chapter 4 and implemented in CUBIT [114] for boundary-layer meshing. The quality of the wedges was measured using their aspect ratio (AR), where it is the ratio between the longest and shortest edge lengths of an element. The quality of the tetrahedra was measured by their

maximum dihedral angle (MDA). The number of wedge and tetrahedral elements and their quality can be seen in Table 5-1.

Table 5-1: List of the elements and their quality for the aneurysm models.

	Wall	Interior		Quality	
Aneurysm	# Wedge	# Wedge	# Tet	AR	MDA
Simplified Aneurysm	5296	39720	40081	2-63	138
Model A	15564	120840	55186	3-374	147
Model B	8284	64410	21378	2-433	140
Model C	26064	200160	105812	3-763	150

The FSI simulations themselves were run with ANSYS® and ANSYS®, CFX™. The blood flow was approximated as a Newtonian fluid with a dynamic viscosity of $\mu = 3.85$ cP and solved using a shear stress transport model. The velocity profiles for the simplified aneurysm and the patient-specific models were different and will be described in their respective sections. The vessel wall was treated as an isotropic material with a Young's modulus of $E = 1.0$ MPa, a density of $\rho = 1055$ kg/m^3, a Poisson's ratio of $\nu = 0.45$, and the ends were fixed in place.

5.1 A Simplified Aneurysm Model

The simplified aneurysm model was shown in Figure 3-1 and the results are in Figure 5-2. The healthy geometry for the AAA was a cylinder with a diameter of 2 cm and a length of 24 cm. The aneurysm, having a diameter of 6 cm, was placed in the center of the healthy vessel

with an offset from the axis of 0.75 cm. The initial wall thickness was calculated to be a constant 1.50 mm, 15% of the healthy radius. After solving for the equivalent wall thickness, the minimum thickness was found to be 0.22 mm, with an average of 1.11 mm, the thickness distribution can be seen in Figure 5-2(a).

The FSI analyses were run to compare the wall stresses and mesh displacement between the uniform and equivalent wall thicknesses. A simplified representation of the cardiac cycle, Figure 5-1(a), was used to provide boundary conditions giving an inlet velocity with a peak of 31 cm/s at 0.3 s and an outlet pressure with a peak of 118 mm Hg at 0.4 s.

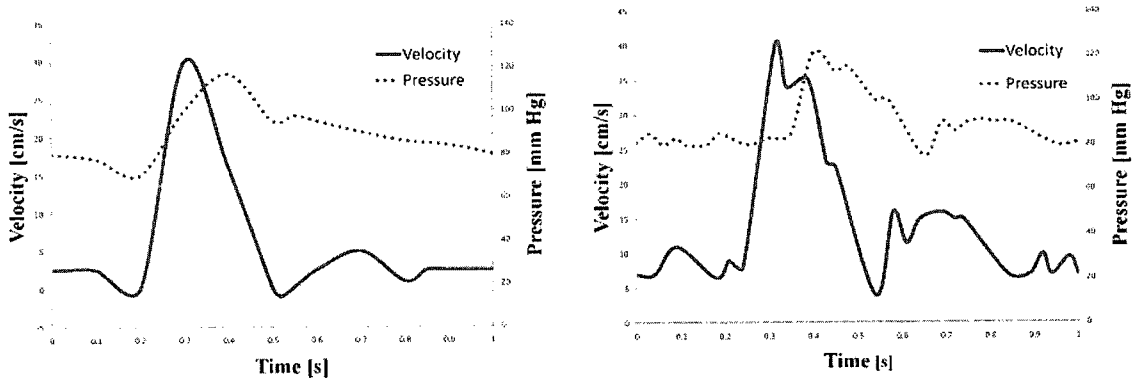

(a) Cycle for AAA **(b) Cycle for cerebral aneurysm**

Figure 5-1: The cardiac cycles used in the FSI analyses

The analysis was first performed on the geometry with a constant wall thickness (1.5 mm). With a pulsatile flow the maximum von Mises stress was 0.31 MPa and occurred on the anterior and posterior regions of the aneurysm, Figure 5-2(b). The second simulation was run using the equivalent wall-thickness and resulted in the maximum stress of 1.04 MPa at about 0.4 s and can be seen in Figure 5-2 (c). Using a variable wall thickness produced a 335% increase in the wall stress even though the aneurysm geometry was unchanged. These

results are similar to work by Scotti, where their model had a uniform wall 1.5 mm thick, and a variable wall-thickness that transitioned between 0.5-1.5 mm, inversely proportional to the local radius of the aneurysm [73,74]. In [73], the maximum von Mises stress increased by 300% for an aneurysm of the shape and size presented here, with the same locations for maximum stress. The slight difference in wall stress between this thesis and [73], is attributable to the thinner equivalent wall thickness.

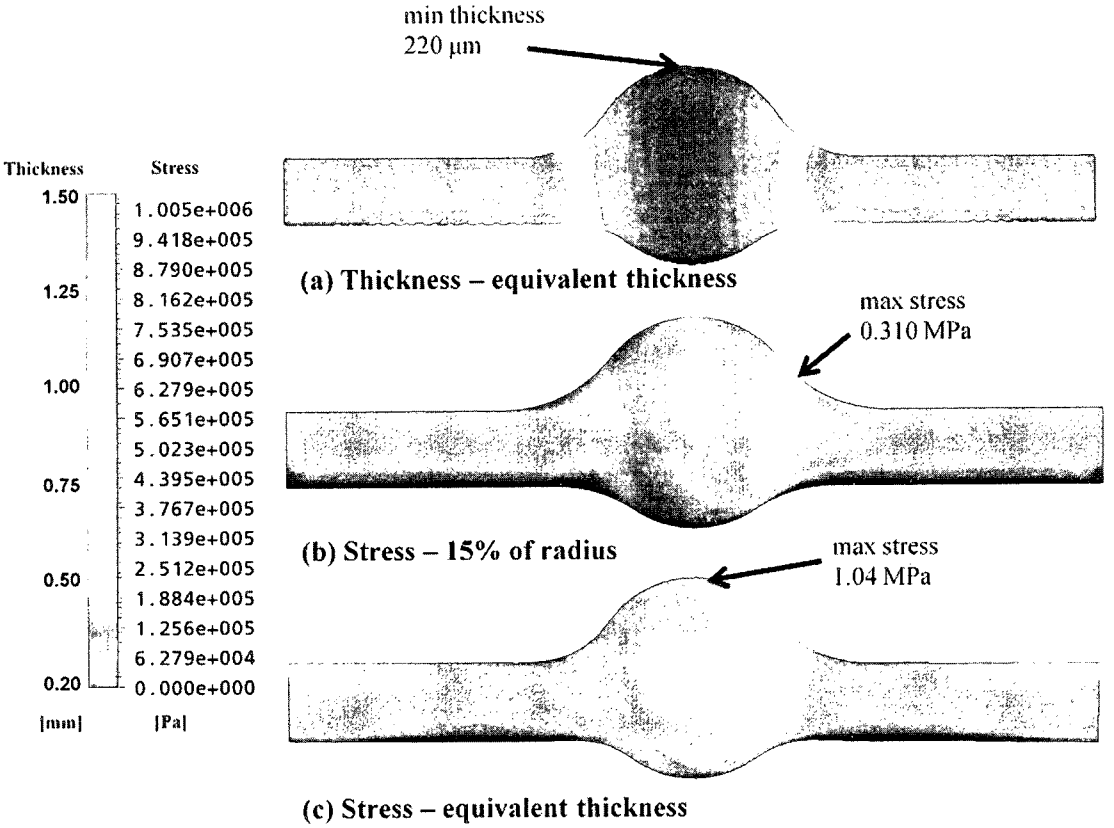

Figure 5-2: Maximum von Mises stress for uniform and equivalent wall thicknesses

5.2 Patient-Specific Cerebral Aneurysms

The three patient-specific cerebral aneurysm models were created from medical imaging data using on octree-based method [52,79], and the equivalent wall-thickness was calculated with the presented method. The healthy surfaces for Models A, B, and C can be seen in Figure 5-

3(a--c) with the deformed and relaxed surfaces in Figure 5-3(d--f), and the cross-sections of the fluid and solid meshes used in the FSI simulations in Figure 5-3(g--i).

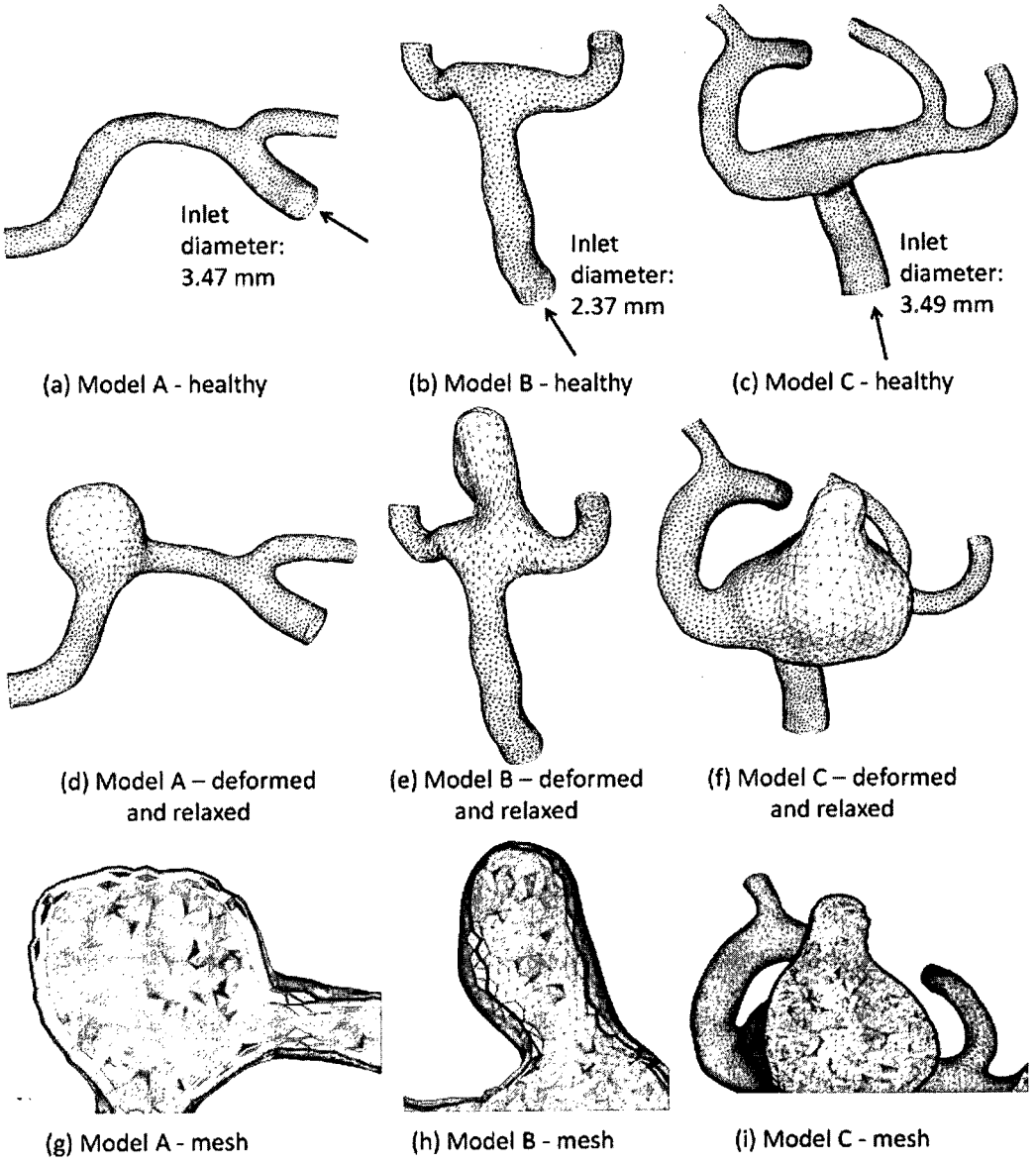

Figure 5-3: Original and deformed meshes for patient-specific cerebral aneurysms.

Of the three patient-specific models used, the aneurysm in model A did not form at the bifurcation and model C has a secondary protrusion, a bleb, on the aneurysm. Models A

and C were presented in [6] using a wall-thickness of 20% of the radius at the boundaries, with the thickness for the remainder of the model being solved with the Laplace equation. The same percentage was used to determine the initial thicknesses for this paper. As shown in Figures 5-4, 5-5, and 5-6, using the equivalent wall-thickness leads to Model A having a minimum thickness 16.4% of its original after the parameterization and spring relaxation, Model B having a minimum of 12.2% the initial, and Model C having a wall-thickness that was 12.0% the starting value; all the percentages are relative to the original thickness at the same location. The average thickness over the aneurysm domes were 73 μm, 80 μm, and 71 μm respectively, and are within the average values given by [7,18] (50--100 μm). The minimum wall-thicknesses also lies within the 16--38 μm range MacDonald measured for the wall near rupture sites on cerebral aneurysms [32]. As expected, the blood-vessel wall becomes dramatically thinner in the dome of the aneurysm.

While the wall shear stress plays an important role in the growth of cerebral aneurysms, the maximum tensile stress will determine its potential for rupture [5,6]. Two sets of simulations were performed to compare the stresses of the equivalent wall thickness with those using the initial, 20% thickness. When running the FSI simulations, the patient-specific cerebral aneurysm models required slightly different flow conditions than the simplified aneurysm because of their location in the body. The blood flow in the brain has a velocity that varies between 4--41 cm/s and a pressure with a range of 75--121 mm Hg [7], where an approximate phase shift of 0.08 s is used [115]. Peak systole occurs at 0.32 s. The thickness and stress results are catalogued in Table 5-2 with select results from literature shown in Table 5-3. The percent difference for the minimum thickness is with respect to the initial thickness at the same location, and the average thickness is calculated over the entire dome.

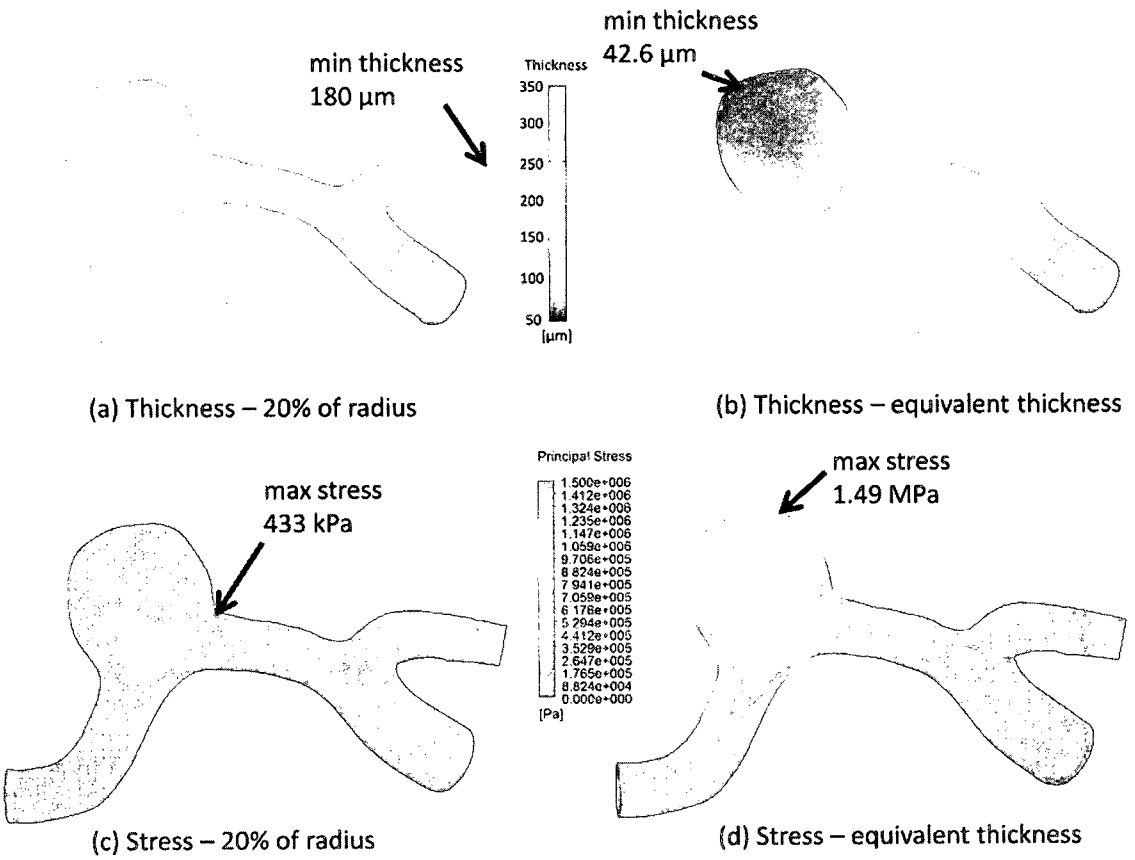

Figure 5-4: Deformation and analysis of patient-specific Model A

The maximum, absolute principal-stress during peak systole for the initial-thickness of Models A, B, and C were 433 kPa, 484 kPa, and 508 kPa, respectively, see Figures 5-4(c), 5-5(c), 5-6(c). These are of the same order as the values for Models A and C found in [6]. The differences in maximum stress may primarily be attributable to the boundary conditions, with the addition of prestress in [6] playing a factor as well. Using the equivalent wall-thickness, Model A had a maximum value of 1.49 MPa, Model B with 0.986 MPa, and Model C was 2.24 MPa, and plots of the maximum absolute principal stress are shown in Figures 5-4(d), 5-5(d), 5-6(d). When compared against the 20% thickness, the thinner, equivalent wall-

thickness produces a striking increase in the maximum principal stress. The maximum stresses achieved with the equivalent wall-thickness fall well within a reasonable bound for cerebral aneurysms [32,45,66,116,117].

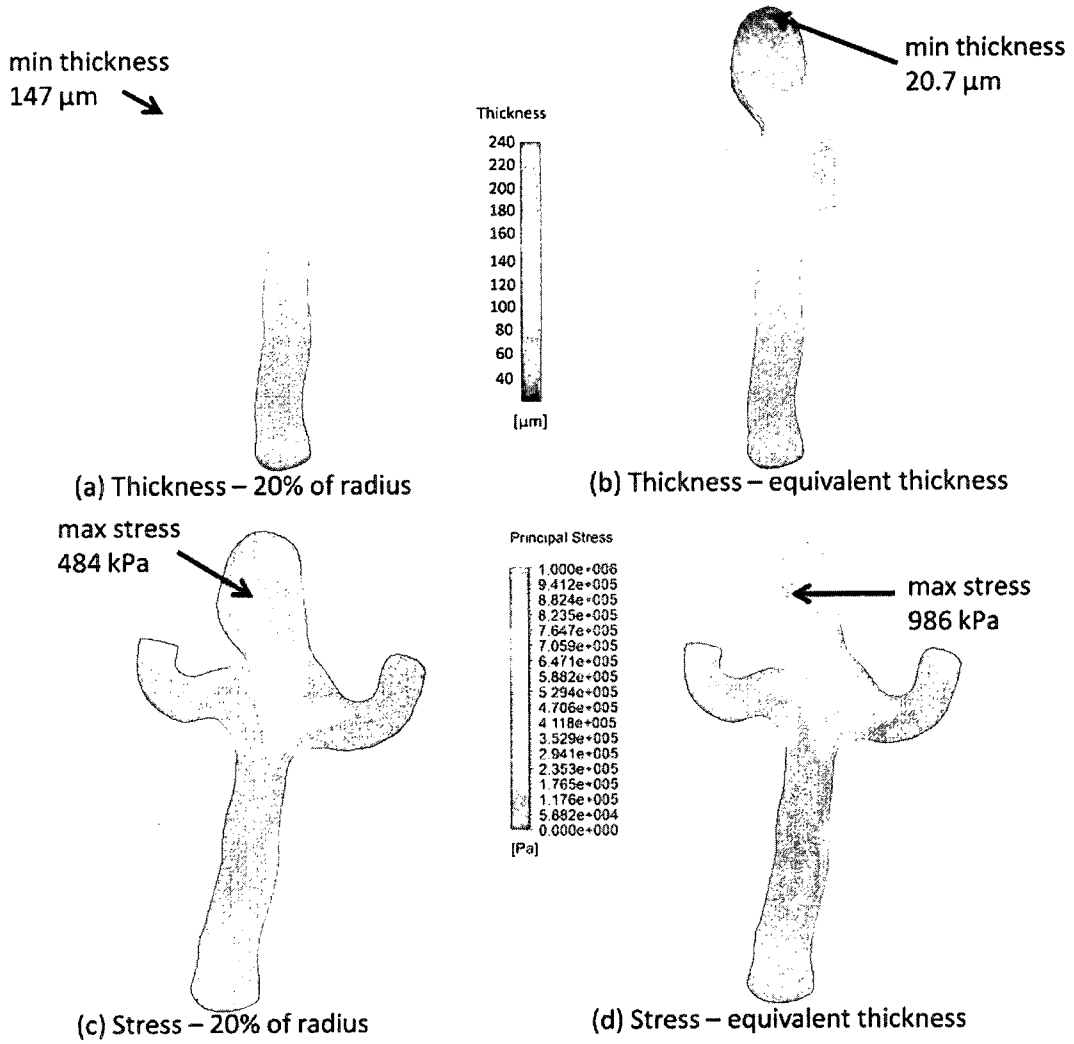

Figure 5-5: Deformation and analysis of patient-specific Model B

The maximum stress results fall well within a reasonable bound for cerebral aneurysms. Using a uniform wall-thickness of 86 μm, Valencia *et al.* found a maximum stress of 0.851 MPa and 1.11 MPa while changing the Young's Modulus from 7-10 MPa [66]. Zhou

et al. found a peak first-principal stress of 450 kPa, while using a non-linear wall with a constant thickness of 100 μm [118], and Isaksen *et al.* show a maximum stress of 500 kPa with a wall 150 μm thick [57]. Ma *et al.* used an anisotropic, non-linear wall that is 86 μm thick, but achieve a maximum stress of 0.310-1.06 MPa between 27 models [116].

Table 5-2: Summarization of stress and thickness results for the aneurysm models.

Aneurysm	Maximum Stress		Equivalent Thickness		
	20% [MPa]	Equivalent [MPa]	d_{init} [μm]	d_{min} [μm]	d_{avg} [μm]
Simplified Aneurysm	0.31	1.04	1500	220 (15%)	1110
Model A	0.43	1.49	260	43 (16%)	73
Model B	0.48	0.99	170	21 (12%)	80
Model C	0.51	2.24	190	23 (12%)	71

Table 5-3: Summarization of the stress and thickness results from select clinical literature.

	Maximum Stress	Thickness	
	[MPa]	d_{min} [μm]	d_{avg} [μm]
Raghavan [45] AAA	0.34-2.35	230	
MacDonald [32] Cerebral	0.73-1.9	16-38	
Humphrey [5] Cerebral	1-10	30	
Abruzzo [18] Cerebral			51

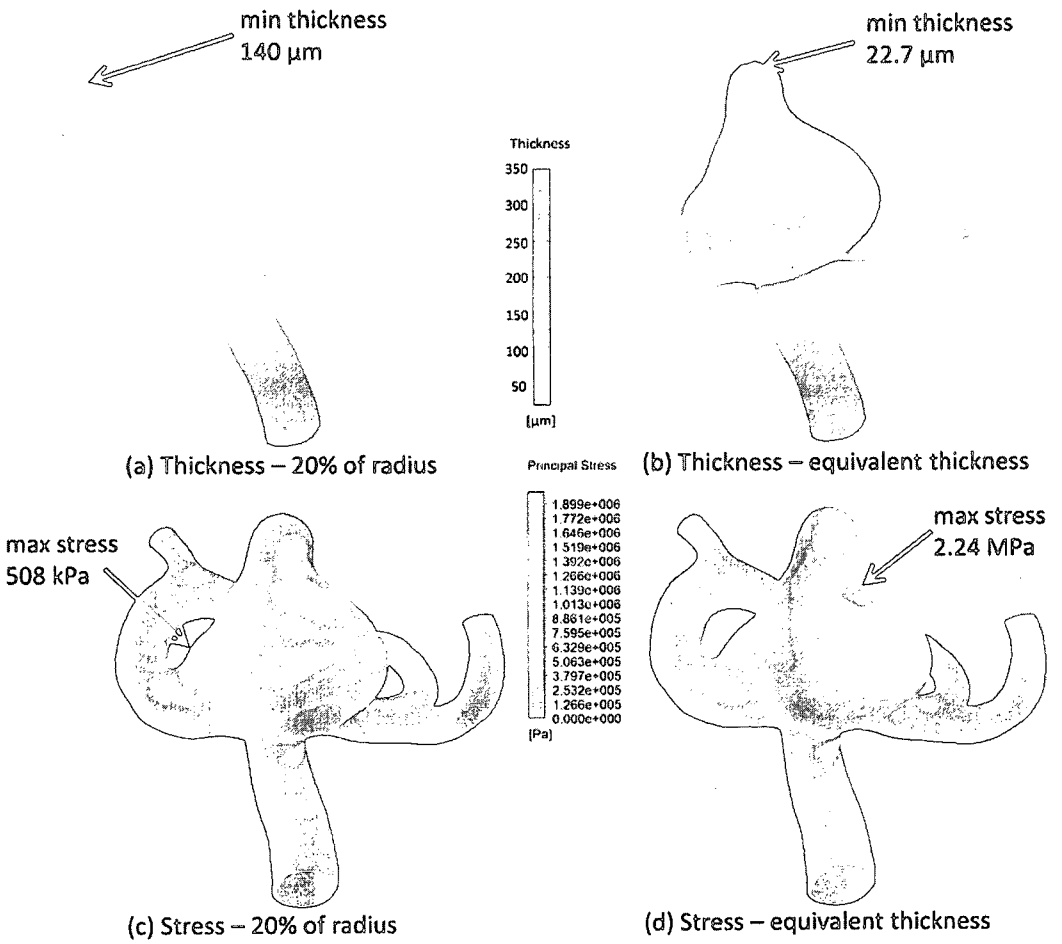

Figure 5-6: Deformation and analysis of patient-specific Model C

From the principal stress results the following can be observed: (1) using a uniform thickness overestimates the strength of the blood vessel wall; (2) the location of maximum stress may change when the equivalent wall-thickness is adopted (and is likely to move onto the aneurysm dome); and (3) the location of maximum stress may not coincide with the location of minimum wall-thickness. As can be seen from these three models, the wall-thickness rapidly shrinks over the dome of the aneurysm, starting near the neck of the aneurysm. When 20% of the radius is chosen as the wall-thickness, the maximum stress in Models A and C is located on the neck of the aneurysm, which coincides with where the

gradient of the thickness is highest in the proposed method, making the stress susceptible to change. However, the maximum stress in Model B is already located in the dome, as shown in Figure 5-5(c), which might explain its limited motion. When the equivalent wall-thickness is used, a maximum stress is obtained that is, on average, 330% larger than when the initial wall-thickness is used, and are located on the aneurysm dome in all three models. As stated in [5,6], the maximum tensile stress determines the potential for rupture, with rupture generally occurring on the dome of the aneurysm [19]. Therefore, compared to using a uniform, 20% of the radius, as the wall-thickness, using the equivalent wall-thickness gives a much more accurate prediction of the rupture site.

It needs to be reminded that the proposed method creates an *equivalent* wall-thickness. While it represents a weakening wall globally, it does not fully capture any local changes in material strength e.g. scarring, inflammation, and plaquing. According to [119] these confined changes have only a minor impact on the stress distribution and magnitudes. However, using a significantly thinner wall with the proposed method, material variations may have the potential to affect the location of the maximums and site of rupture.

5.3 Summary

Through the FSI simulations, it can be seen how significant a role the aneurysm wall-thickness plays in determining the deformation and maximum wall stress. Instead of using a constant thickness, the proposed mesh deformation method provides a way to calculate the wall-thickness in a physically meaningful manner. This provides an improved model for use within finite element solvers. The addition of a tool to aid in the generation of boundary-layer meshes, reduces the total number of elements required for a mesh of the fluid domain, and improves the overall quality of the mesh within the boundary-layer region.

Chapter 6

The Addition of Anisotropy

Adding anisotropic material properties to simulations of biological models is difficult. Even though blood-vessel tissue has components in the axial and circumferential directions, it is difficult to define on most models. Complex ones, like the heart and aneurysms, have regions of ambiguity where it is tricky to decide which direction is which.

This chapter presents a method to define the material directions on aneurysm models by extending the capabilities of the mesh deformation described in Chapter 3. The directions of principle-curvature found on a healthy blood-vessel model give a good indication of the axial and circumferential directions, and these can be moved to the aneurysm model. With these, the spring relaxation in Section 3.2 can be improved, and material directions can be added to FEA and FSI solvers.

6.1 Material direction from surface curvature

Though seemingly obvious, the material directions for a model need to be evaluated before they can be applied to a simulation. Using incorrect directions will influence the outcome of an analysis and result in false conclusions being made about the system. For healthy blood vessel tissue, the material directions are closely aligned with the axial and circumferential directions of the blood vessel; however, choosing those for a model is not straight forward. Moreover, the directions become increasingly difficult to determine when the tissue has stretched in unknown ways over an aneurysm.

Determining the axial and circumferential directions is intuitive for a linear cylinder; where the axial component points in the same direction as the centerline of the cylinder and the circumferential component is orthogonal to both the axial direction and the local normal of the surface. These definitions are extendable to pipe-like objects, as seen in Figure 6-1, where the axial direction now takes the local tangent of the centerline. This methodology is just beginning to be used in simulations where a "spine" is created from the centerline and projected onto the surface of the model [30,34,36,80]. Although this does provide a good approximation of the material directions, it does not take into account the complex geometry of an aneurysm or the deformations it underwent. In the end, the directions determined for an aneurysm are nearly identical to the ones created for a healthy model using the same centerline.

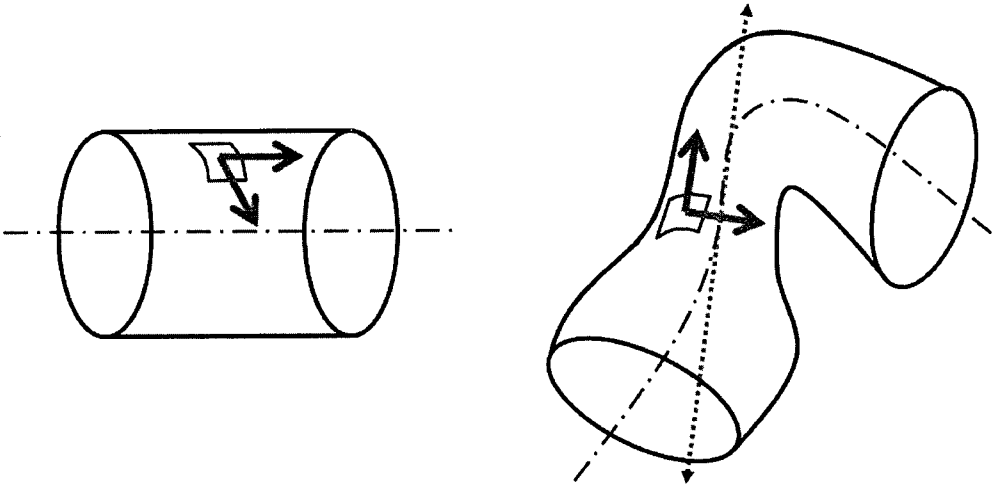

(a) Cylinder **(b) Pipe-like object with tangent-line (dotted)**

Figure 6-1: Axial and circumferential directions for pipes

As shown in Chapter 3, starting from a healthy model provides information that cannot be found with an aneurysm model alone, i.e. the thickness. Following this same

reasoning, the anisotropic, material directions for an aneurysm should be evaluated first on a healthy model. Instead of depending on the quality of the centerline, the principle-curvatures from the healthy blood-vessel will define the material directions. The directions of principle-curvature are defined locally at every point and can be moved with the deforming mesh onto the aneurysm model.

The use of the principle curvature to define the material directions was based on the type of geometry being used. Biological models are smooth and rarely contain sharp features. This means the curvature directions can be relied on to not rapidly change. Additionally, because the vascular system is comprised of "narrow" tubes, the circumferential component is almost always guaranteed to be in the direction of highest curvature. Only in sharp corners, e.g. where a blood-vessel branches, might the axial direction have a higher curvature. This method is applicable to the bulk of an aneurysm models, but in regions where the curvatures are similar, like the dome of an aneurysm, ambiguity could prevent the choice of directions. These regions of ambiguity are where having the correct material direction is critical, and therefore calculating the directions cannot be done on the aneurysm model. Also, since the wall is being stretched, it is unlikely the fibers will remain perfectly axial and circumferential; though the material directions will remain orthogonal to each other. As described in Chapter 2 the fibroblasts will try to keep the collagen parallel with its neighbors, so there will not be a significant realignment due to any deformations. Thus the anisotropic directions should be found on the healthy model and then moved onto the aneurysm.

The directions of principle-curvature are found through the extended quadric method presented in [77,120,121,122]. The extended patch modification from Garimella and Swartz

[122] is also used to improve the algorithm near boundaries. This algorithm is applicable to models created from mesh elements, or facet geometry. For each node $\boldsymbol{p}$ on S_0, a quadric surface is fit over the local patch of elements through a least-squares solution of Equation (6.1), where a, b, c, d, and e are the coefficients being solved for, and $\boldsymbol{X'}$, $\boldsymbol{Y'}$, and $\boldsymbol{Z'}$ are the component directions of the local coordinate frame at the node.

$$\boldsymbol{Z'} = a\boldsymbol{X'}^2 + b\boldsymbol{X'}\boldsymbol{Y'} + c\boldsymbol{Y'}^2 + d\boldsymbol{X'} + e\boldsymbol{Y'} \tag{6.1}$$

The local coordinate frame is defined as follows:

1. $\boldsymbol{Z'}$ is the regularized surface normal, $\hat{\boldsymbol{n}}$, at $\boldsymbol{p}$, and can be approximated as the average of the neighboring element normals.
2. $\boldsymbol{X'}$ takes the direction of the global X-axis projected against the plane defined by $\hat{\boldsymbol{n}}$ as defined in Equation (6.2), where I is the 3x3 identity matrix and $\hat{\boldsymbol{\imath}}$ is the global x-axis.

$$\boldsymbol{X'} = \frac{(\mathrm{I} - \hat{\boldsymbol{n}}\hat{\boldsymbol{n}}^T)\hat{\boldsymbol{\imath}}}{\|\mathrm{I} - \hat{\boldsymbol{n}}\hat{\boldsymbol{n}}^T\|\hat{\boldsymbol{\imath}}} \tag{6.2}$$

3. $\boldsymbol{Y'}$ is orthogonal to both $\boldsymbol{X'}$ and $\boldsymbol{Z'}$.

At least five points, in addition to the node in question, are needed to solve the least-squares problem due to the number of variables in Equation (6.1). This is typically satisfied

by the collection of nearest neighbors; however, if there are not enough points it should be expanded to the 2-ring neighbors. Also, the quadric surface may not properly capture the curvature near boundaries, where only *half* of a patch is present. In this case all the neighbors are mirrored about $\boldsymbol{p}$. The neighbors are transformed into the local frame with Equation (6.3), where $\boldsymbol{x}$ and $\boldsymbol{x}'$ are coordinates in the global and local frames, respectively, and rotation matrix is $\mathrm{R} = [\boldsymbol{X}', \boldsymbol{Y}', \boldsymbol{Z}']^T$.

$$\boldsymbol{x}' = \mathrm{R}(\boldsymbol{x} - \boldsymbol{p}) \tag{6.3}$$

The linear terms of the extended quadric allow the surface normal to be updated through Equation (6.4), and will in turn update $\boldsymbol{X}'$ and $\boldsymbol{Y}'$.

$$\hat{\boldsymbol{n}} = \frac{[-d, -e, 1]^T}{\sqrt{(d^2 + e^2 + 1)}} \tag{6.4}$$

Iterating over a patch until $\hat{\boldsymbol{n}}$ converges yields a more accurate estimation of the principle-curvature directions. Figure 6-2 shows the improvement in curvature calculations for a unit-sphere when using the extended quadric method. The quadratic terms of Equation (6.1) define a shape operator for the patch, Equation (6.5) [120], and the eigenvectors of this matrix are the directions of principle-curvature. The eigenvalues are the principle-curvature values.

$$S = \begin{bmatrix} 2a & b \\ b & 2c \end{bmatrix} \tag{6.5}$$

These vectors need to be transformed back into the global frame by multiplying by the inverse of the updated rotation matrix.

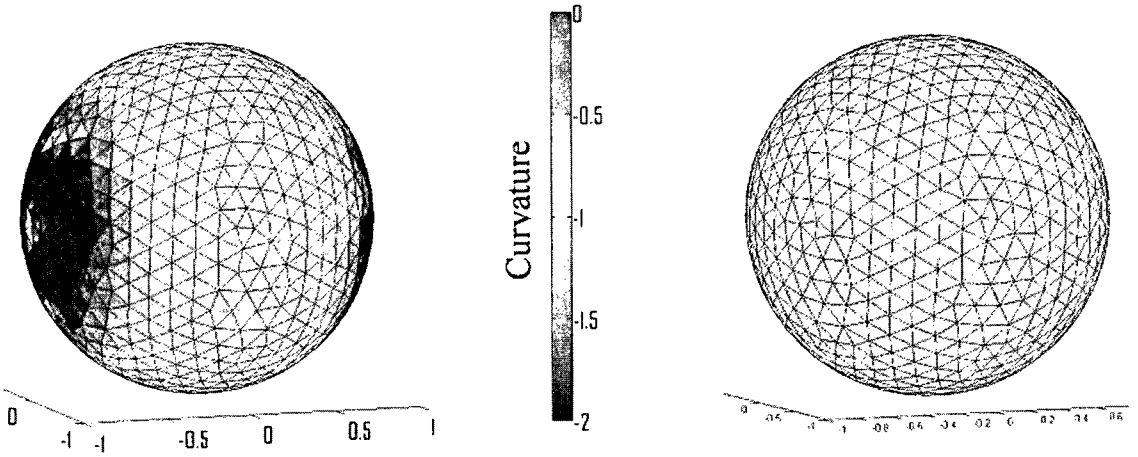

(a) Mean curvature using quadric method

(b) Mean curvature using extended quadric method

Figure 6-2: Comparison of basic versus extended quadric method

Every node $\boldsymbol{p}$ in the mesh on S_0 now has a pair of material directions that correspond to the axial and circumferential directions. The circumferential component is set to the direction with the largest curvature value; however, in some cases this choice may be incorrect. In order to ensure no rapid changes in the material directions have emerged, a couple iterations of Laplacian smoothing are applied. Examples of the curvature directions, as evaluated from the directions of principle-curvature, can be seen in Figure 6-3(a)(b).

As Chapter 2 stated, the true material directions are not quite axial or circumferential. This orientation offset can easily be achieved prior to transforming the directions back to the global frame. Rotating around the z-axis, the surface normal, by an angle will realign the fibers to their new orientation. This can be seen in Figure 6-3(c), where an offset angle of 40° was applied. These directions will further influence how the material is stretched.

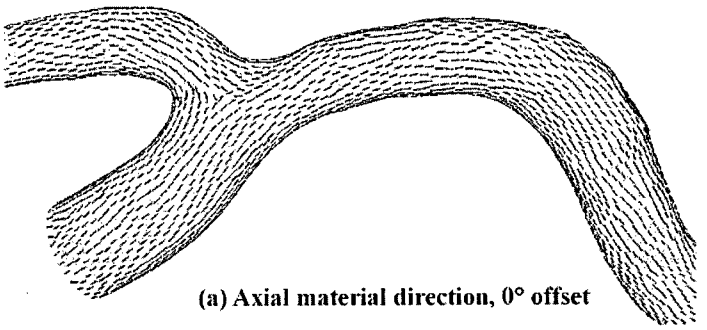

(a) Axial material direction, 0° offset

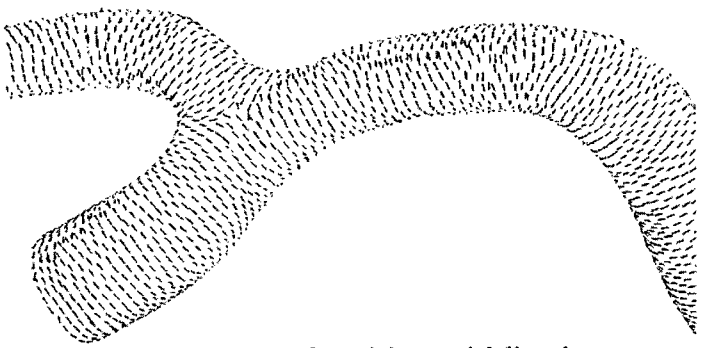

(b) Circumferential material direction, 0° offset

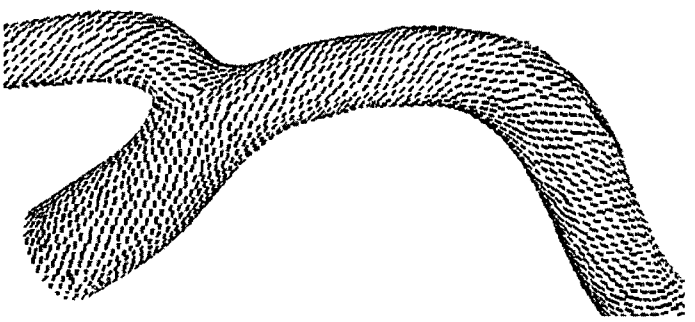

(c) Axial material direction, 40° offset

Figure 6-3: Model A material directions as found by the principle-curvature

6.2 Using Anisotropy for Spring Relaxation

Once the material directions have been found for S_0, they need to be moved to S_2 in order to be used in any analysis. However, the aneurysm is the deformed blood-vessel *after* loading, and so directly transforming the coordinate systems is not sufficient. In order to include anisotropy in the spring-relaxation step from Section 3.2, the material directions need to be embedded in each element. In particular, the individual springs need to be decomposed into its contributions from both component directions.

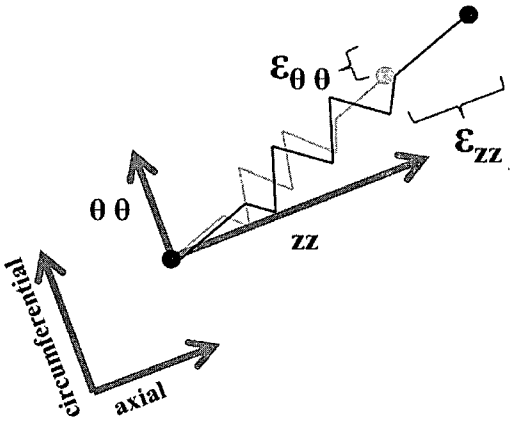

Figure 6-4: Component breakdown of spring into material directions with strains

The springs are split into axial and circumferential components through the dot-product with the material directions of S_0, as illustrated in Figure 6-4. Strain experienced by a spring can now be expressed by its contribution in both of the component directions. In addition, the angle of the spring with respect to the axial direction, φ_i, needs to be stored in order to extract the material directions from the springs after deformation. Returning to the material model of Equation (2.1), the spring stiffness can be rewritten as Equation (6.6),

where ε_{zz} and $\varepsilon_{\theta\theta}$ are the axial and circumferential strains for each spring, respectively, a_1, a_2, a_4, and C are material constants, and l_{ij} is the current length of the spring.

$$K_{ij} = \frac{C}{l_{ij}} e^{a_1\varepsilon_{\theta\theta}^2 + a_2\varepsilon_{zz}^2 + 2a_4\varepsilon_{\theta\theta}\varepsilon_{zz}} \tag{6.6}$$

Using Equation (6.6) as the new stiffness equation, the resultant deformation takes into account the non-linearity and the directionality of the tissue. Proceeding with the remainder of the process in Section 3.2, the spring system is relaxed and terminated under the same conditions.

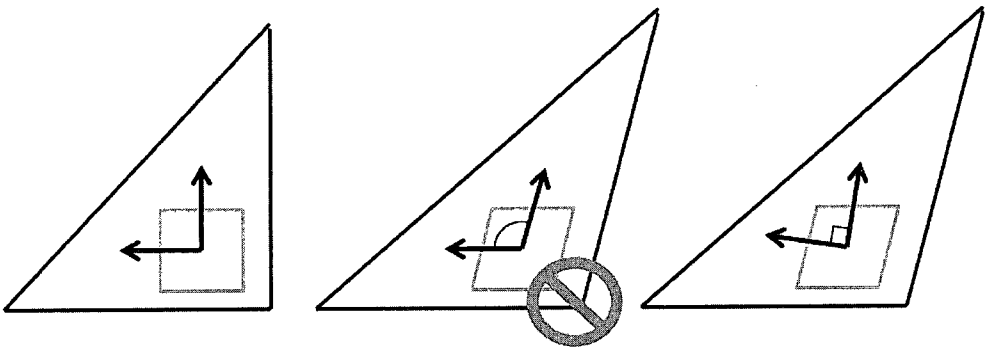

(a) Original element with material directions shown for a patch

(b) Update of *Hookean* material-directions for skewed element

(c) Update of collagen material-directions for skewed element

Figure 6-5: Change in material directions after deformation of element

By tying the material directions to each edge while the spring-system is relaxed, they will begin to orient themselves toward the largest loads as the elements are stretched. However, because collagen is a linear fiber the material directions will remain orthogonal as the tissue is strained, see Figure 6-5(c); unlike most materials where they would skew under a

shear, see Figure 6-5(b). If the axial and circumferential components were found through a centerline and attached to S_2 before the spring relaxation, it would inhibit the mesh and material directions from moving freely and deforming the way it did. Decomposing every spring into its component parts at the start means the strain do not need to be continually split during each iteration.

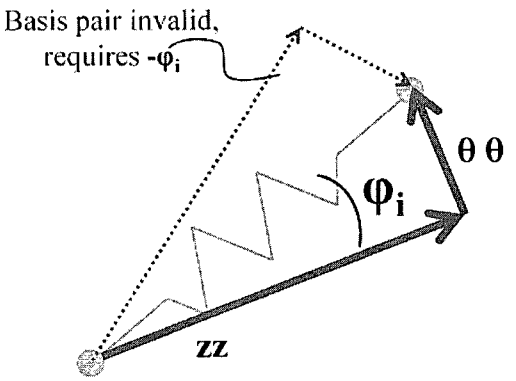

Figure 6-6: Reconstitution of the material directions based on spring components

6.3 Reconstituting the Material Directions

Since the new material directions aided in the spring relaxation and have been realigned according to the deformation, they should be representative of the anisotropy of the tissue and usable in a finite element or FSI simulation. Reversing the steps in Section 6.2, the components associated with each spring need to be reconstituted into an individual vector. Unfortunately, the components themselves are not sufficient by themselves and create a pair of solutions; this is why the original orientation of an edge, with respect to the axial direction, was stored. Using φ_i, the correct orientation can be found and the "axial" direction chosen. The "circumferential" direction remains orthogonal to both the axial

direction and surface normal. Remember that even though the material directions are represented by vectors, the material will stretch identically in both the positive and negative direction, so the sign is negligible.

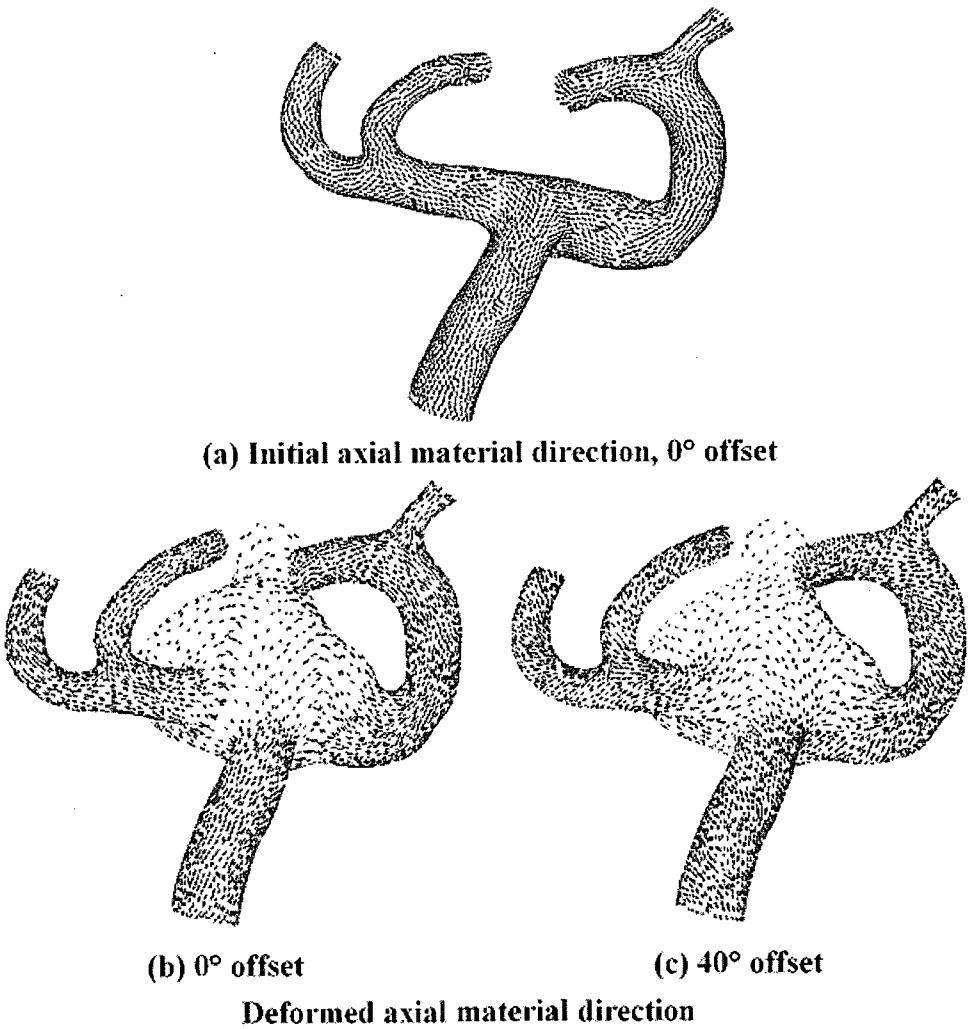

Figure 6-7: Model C deformed material directions with 0° and 40° offset

It becomes apparent, after visualizing the anisotropy, that the vessel tissue does not remain purely axial and circumferential as it stretches. The "axial" directions for the deformed Model C is shown in Figure 6-7, showing the effect of both a 0° and 40° offset.

As collagen is replaced the fibroblasts will try to maintain the parallel arrangement of the fibers. This means that the collagen is unlikely to return to an axial and circumferential direction until some large amount of time after the aneurysm has grown, especially in the timeframe of the initial formation. Also, starting the fiber orientation at some offset can significantly alter the local arrangement of the material directions, as seen in the comparison of Figure 6-7(b)(c).

6.4 Isotropy versus Anisotropy Continued

With the addition of anisotropy into the presented mesh deformation method, the accuracy of the calculated wall thickness should improve and be more physically meaningful. The question arises of whether or not including anisotropy is significant. If simulation results using anisotropy show substantially different wall stresses, clinicians will be able to provide better diagnostic, preventative, and curative measures. If not, the computational cost of including it may outweigh the benefits.

The minimum thickness for patient-specific Model A using isotropic springs was 16.4% smaller than its original thickness while the anisotropic springs the minimum thickness was 15.6% thinner. The minimum values are nearly identical and the location did not move. The final meshes shown in Figure 6-8 also look similar; however when anisotropy is factored in, the elements on the aneurysm are slightly stretched in the circumferential direction. The transition regions around the aneurysm also show a clustering of elements in the axial direction. Yet, when looking at what contributes to stress values, the minimum wall thickness plays a dominant role.

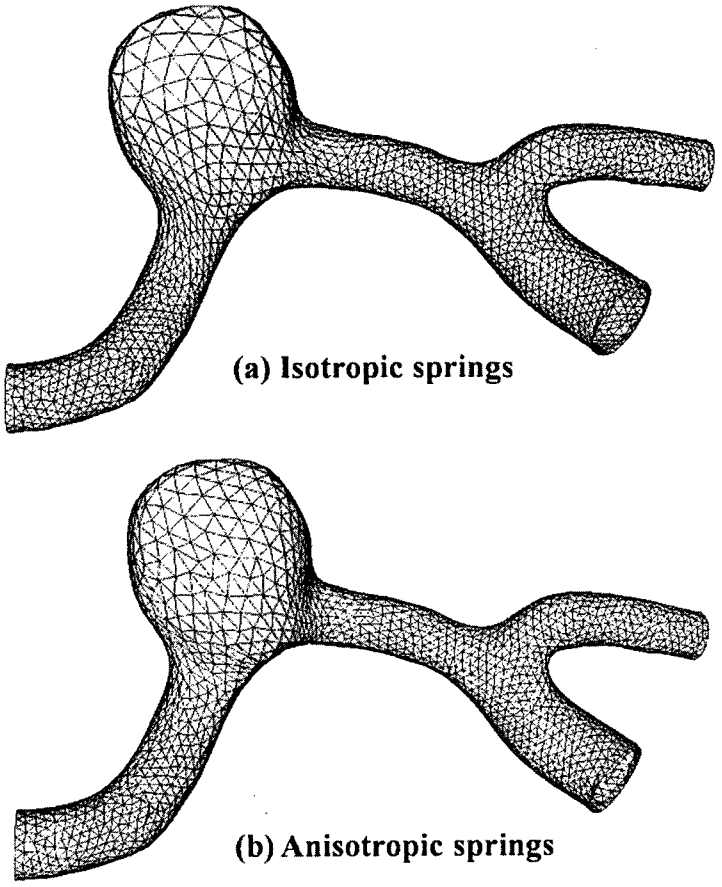

Figure 6-8: Isotropic versus anisotropic comparison on aneurysm

A few more details can found when comparing the ratio of wall thickness for both models. A plot of the thickness ratio between the anisotropic and isotropic models is shown in Figure 6-9. As expected, the majority of the mesh is unaffected by the addition of anisotropy; only over the aneurysm does it factor in. More importantly though, the deviations in thickness may be small, but they are clustered. The clustering means larger patches of the aneurysm are weaker or stronger and could change how the model deforms under load. Undergoing a mildly different deformation could alter the maximum wall stress,

and will make a difference when simulating the outcome of a procedure, like the placement of a stent.

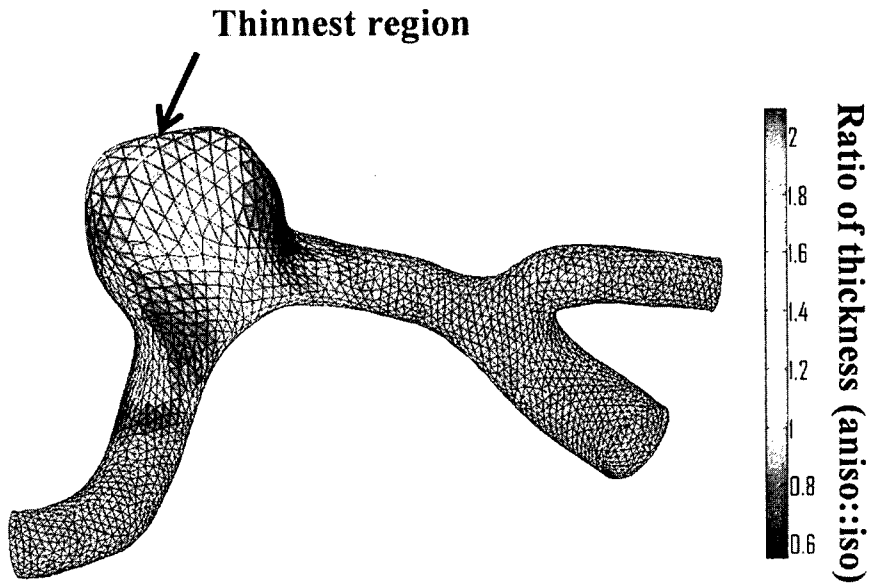

Figure 6-9: Plot of thickness ratio at every node on patient-specific model A

While the material directions have been difficult to apply toward a simulation, there has been some work to find them via an inverse method [116,123]. Solving an inverse finite element method problem they try to determine the original configuration, i.e. displacement, loads, and stresses, from a known final model and the loads on it. The material directions are chosen to align with the directions of principal stress. Since the highest stresses typically occur near regions of high curvature, the directions tend to coincide with the principal curvature as well; though these results still assume a uniform wall thickness.

The material directions determined through the spring relaxation appear to produce a similar distribution. This is a result of the deformation stretching the material, while it is still

unmodified in the healthy region. Given that the magnitude of the curvature over the aneurysm can no longer be used to quantify the axial and circumferential directions, it seems apparent that moving them from the healthy model provides the most accurate distribution and retains a smooth flow of the material properties.

6.5 Summary

This chapter presented an extension method to include anisotropy in the mesh deformation techniques of Chapter 3. Using the principle-curvature directions from the healthy blood-vessel model, a good estimate of the axial and circumferential directions can found. This allows the springs to deform in an anisotropic fashion as the mesh is deformed. While the minimum thickness does not substantially change, the trends over the entire model hint the maximum stresses will. Presented in Section 6.2, extending the anisotropic material directions to a finite element package will provide a better idea on the significance of anisotropy in simulating biological models.

Chapter 7

Conclusion

The explosion in computational power over the last couple decades has pushed, what was once the sole prevue of engineers, into the forefront of a wide number of disciplines. Structure and fluid simulations are no longer restricted to solving the failure of a piston or the lift of an airfoil. For the medical community this has meant a potential renaissance in understanding disease progression and the human body. It has also brought the possibility of simulating surgeries, before they even happen, with the hope of improving patient outcomes.

However, the introduction of computational analysis *outside* its primary bubble has also meant that some tools have been pushed the limits of what they are capable of. This is readily seen in the analysis of aneurysms, where it has moved from CFD simulations of a cylinder to large FSI analyses of the vasculature using non-linear walls with a resistance pressure for the outlets. Even though the bulk of the research has worked toward improving the accuracy of the simulations and the time required to run them, the majority of the data is still approximated. The wall thickness, the prestress of the vessel tissue, the material directions, the distribution of material properties, etc are not known and cannot be found *in vivo* for patient-specific aneurysms. The former being a limitation of the imaging techniques available, while the remainder not being measurable until the aneurysm has been excised, and still only in a limited fashion. It is known, however, that the wall of an aneurysm weakens as it grows and unless a simulation takes that into account, it cannot provide a researcher or a medical professional with accurate results.

7.1 Contributions

This thesis has presented new tools for improving the accuracy of fluid-structure interaction analyses of patient-specific cerebral aneurysms. Through these contributions, information about the material and state of the aneurysm can be used and that has up until now been unavailable. The contributions are:

(1) a framework to calculate an equivalent wall thickness for any aneurysm,

(2) a boundary-layer mesh sizing-function,

(3) a means to determine the anisotropic material directions over any aneurysm, and

(4) an implementation of each to allow FSI simulations of patient-specific models.

The equivalent wall thickness captures the weakening of the vessel wall without relying on image data. The thickness is found by deforming the mesh from a healthy model onto the aneurysm and then allowing the spring system to relax. It takes into account the non-linearity of the tissue to better approximate the elastic, stretching nature of the vessel wall. Additionally, the algorithm has been created in such a way that it can be calibrated as more information becomes known. This will allow the thickness to be changed both globally as a result of the material and locally as a result of the relative strain. For young aneurysms the equivalent wall is a good, though conservative, estimate of the actual wall thickness. As an aneurysm ages it may increase in mass, but will remain a much weaker structure than the surrounding healthy tissue and that is able to be captured by a variable wall thickness.

With its extension to anisotropy, the material directions of the aneurysm wall can be incorporated. This allows the material directions to affect the thickness calculation, but more importantly, it also provides finite element and FSI simulations with more realistic material directions. The anisotropy over the aneurysm is approximated by the principal curvatures of the healthy model with the motion of the springs as they relax. As was shown, the directions do not necessarily align with the axial and circumferential directions after the deformation. Moreover, the collagen fibers can be oriented off the axis by starting from the healthy model.

The addition of a boundary-layer mesh sizing function improves the speed at which a suitable mesh can be created and its quality. By using the medial ball, any advancing front method can know the distance a front is allowed to travel before overlapping with a competitor. This significantly reduces the time it takes to create a mesh on a model with disparate feature sizes. Additionally, anisotropic, prismatic elements can be used, which are superior at capturing the flow than tetrahedra. This improves the accuracy of the result while requiring less time to perform a simulation.

Through these contributions it was shown that the wall thickness plays a significant role in the tensile stresses. The location of the maximum stress moved from the neck of the aneurysm onto the dome, where it was expected and as a result showed a significant increase in the maximum, absolute principal stress when compared against the models currently being used. All of the thickness and stress values fall within what is known experimentally.

7.2 Limitations

There are a few limitations that arise from the assumptions made and the lack of available information. The primary limitation is the idealization of blood vessel tissue, including the

wall always becoming thinner and being uniform in strength; the former has been discussed at length throughout this thesis. While the proposed method tries to capture the weakening of the wall as only a function of the thickness, there will be local variations in the material strength. These changes are caused by scarring of the wall, inflammation of the tissue, plaquing, etc and may affect the stress distribution and site of rupture. As discussed in Section 5.2, [119] showed that local changes in the material strength had little influence on the final stress distribution, but a broader study with the equivalent wall model may show a difference.

Another limitation of the current work is the idealization of the simulation domain. The boundary and loading conditions have been simplified from the environment an aneurysm functions in. Notably missing are any external loads from the intracranial pressure and brain. Also, if this work were to be extended to a broader range of aneurysms, the inclusion of external and internal structures, e.g. bone/spine, intraluminal thrombus, would need to be addressed. Each of these would alter the stress distribution and maximum values. However, even as simulations become increasingly realistic, the results from this thesis, that the model wall thickness plays a critical role in the analysis process, will remain.

7.3 Future Work

That being said, the weakest part of this thesis is the lack of validation with experimental results. Unfortunately this cannot be fully remedied until more data becomes available. Yet, there are a few ways to further improve the soundness of this work. First, more models should be used and simulated to compare against the current body of literature. While this may appear to be repeating what has been done, the addition of more models will show how any of the parameters should be changed and provide a larger statistical pool to weigh

against. Second, when available, the equivalent wall should be compared against the image data. This could provide a rough means to quantify any variation and modify the parameters accordingly; though it needs to be reminded that an increase in the thickness does not necessarily mean an increase in strength, and that the image is likely to have overestimated the actual thickness. Third, while suffering from the same validation problem, the anisotropic material properties should be used in future simulations.

In conjunction with validating the results, the influence of the above limitations should be determined. The impact of changing material properties could be modeled with localized variations in the thickness, i.e. peaks and valleys for pockets of stronger and weaker tissue, respectively. It is already known that including intraluminal thrombuses will reduce the stress in abdominal aortic aneurysms (AAAs) [30,39,124], so adding intracranial pressure, surrounding tissue or organs, and any bones may have a further impact on the stress concentrations.

Even though the focus of this thesis has been on cerebral aneurysms, there are many similarities between them and their larger counterparts throughout the rest of the body. The most significant difference between intracranial saccular and abdominal aortic aneurysms is their pathogenesis, which controls the likelihood of the wall becoming thicker during its growth. Neointimal proliferation, inflammation, and thrombosis coincide with the growth of the AAA and may result in the wall thickness becoming larger than originally [5,22,23]. However, as with the collagen growth in cerebral aneurysms, even though the wall may thicken does not mean it becomes stronger than the healthy vessel. As with cerebral aneurysms, the minimum wall thickness for AAAs is on the order of the image resolution and would still benefit from an equivalent wall thickness. A few AAA simulations have been

performed to categorize the influence of intraluminal thrombuses and show a slight reduction in the tensile stress as it supports some of the load [30,39,124,125,126]. This demonstrates that more than the wall structure should be included if this work were to be expanded for more aneurysm types. Yet, since a AAA is still most likely to rupture near its fundus, the weakening of the wall has to be accounted for in a simulation, and the equivalent wall thickness appears to be an appropriate initial guess.

References

[1] NINDS, *Cerebral Aneurysm Fact Sheet, NIH Publication No. 08-5505*, NIH, 2008.

[2] Y. Bazilevs, M. Hsu, D.J. Benson, S. Sankaran, and a.L. Marsden, "Computational fluidstructure interaction: methods and application to a total cavopulmonary connection," *Computational Mechanics*, vol. 45, 2009, pp. 77-89.

[3] T. Tezduyar, S. Sathe, T. Cragin, B. Nanna, B. Conklin, J. Pausewang, and M. Schwaab, "Modelling of fluid-structure interactions with the space-time finite elements: Arterial fluid mechanics," *International Journal for Numerical Methods in Fluids*, vol. 54, 2007, p. 901–922.

[4] K. Takizawa, J. Christopher, T. Tezduyar, and S. Sathe, "Space–time finite element computation of arterial fluid–structure interactions with patient-specific data," *Commun Numer Methods Eng, published online, doi*, vol. 10, 2009, pp. 101-116.

[5] J. Humphrey and C. Taylor, "Intracranial and abdominal aortic aneurysms: similarities, differences, and need for a new class of computational models," *Annual Review of Biomedical Engineering*, vol. 10, 2008, pp. 221-246.

[6] Y. Bazilevs, M. Hsu, Y. Zhang, W. Wang, T. Kvamsdal, S. Hentschel, and J... Isaksen, "Computational vascular fluid-structure interaction: methodology and application to cerebral aneurysms.," *Biomechanics and modeling in mechanobiology*, 2010.

[7] R. Torii, M. Oshima, T. Kobayashi, K. Takagi, and T.E. Tezduyar, "Influence of wall thickness on fluid-structure interaction computations of cerebral aneurysms," *International Journal for Numerical Methods in Biomedical Engineering*, vol. 26, 2010, pp. 336-347.

[8] S. Scott, G. Ferguson, and M. Roach, "Comparison of the elastic properties of human intracranial arteries and aneurysms," *Canadian Journal of Physiology and Pharmacology*, vol. 50, 1972, p. 328–332.

[9] R. Wulandana and A. Robertson, "An inelastic multi-mechanism constitutive equation for cerebral arterial tissue," *Biomechanics and Modeling in Mechanobiology*, vol. 4, 2005, p. 235–248.

[10] C. Cawley, R. Dawson, G. Shengelaia, G. Bonner, D. Barrow, and A. Colohan, "Arterial saccular aneurysm model in the rabbit," *American Journal of Neuroradiology*, vol. 17, 1996, p. 1761.

[11] P. Canham and G. Ferguson, "A mathematical model for the mechanics of saccular aneurysms," *Neurosurgery*, vol. 17, 1985, p. 291.

[12] P. Canham, H. Finlay, J. Dixon, and S. Ferguson, "Layered collagen fabric of cerebral aneurysms quantitatively assessed by the universal stage and polarized light microscopy," *The Anatomical Record*, vol. 231, 1991, p. 579–592.

[13] M. Kroon and G. Holzapfel, "A model for saccular cerebral aneurysm growth by collagen fibre remodelling," *Journal of theoretical biology*, vol. 247, 2007, p. 775–787.

[14] M. Kroon and G.a. Holzapfel, "Estimation of the distributions of anisotropic, elastic properties and wall stresses of saccular cerebral aneurysms by inverse analysis," *Proceedings of the Royal Society A: Mathematical, Physical and Engineering Sciences*, vol. 464, 2008, pp. 807-825.

[15] S. Baek, K. Rajagopal, and J. Humphrey, "Competition between radial expansion and thickening in the enlargement of an intracranial saccular aneurysm," *Journal of Elasticity*, vol. 80, 2005, p. 13–31.

[16] S. Baek, K. Rajagopal, A. Fellow, J. Humphrey, and M. ASME, "A theoretical model of enlarging intracranial fusiform aneurysms," *Journal of biomechanical engineering*, vol. 128, 2006, p. 142.

[17] J. Suzuki and H. Ohara, "Clinicopathological study of cerebral aneurysms," *Journal of Neurosurgery: Pediatrics*, vol. 48, 1978, pp. 505-514.

[18] T. Abruzzo, G. Shengelaia, R. Dawson 3rd, D. Owens, C. Cawley, and M. Gravanis, "Histologic and morphologic comparison of experimental aneurysms with human intracranial aneurysms," *American Journal of Neuroradiology*, vol. 19, 1998, p. 1309.

[19] T. Crawford, "Some observations on the pathogenesis and natural history of intracranial aneurysms," *Journal of Neurology, Neurosurgery \& Psychiatry*, vol. 22, 1959, p. 259.

[20] W.R. Quadros, "A computational framework for automating generation of finite element mesh sizing function via skeletons," 2005.

[21] W.R. Quadros, K. Shimada, and S.J. Owen, "Skeleton-based computational method for the generation of a 3D finite element mesh sizing function," *Engineering with Computers*, vol. 20, 2004, pp. 249-264.

[22] D.M. Wootton and D.N. Ku, "Fluid mechanics of vascular systems, diseases, and thrombosis.," *Annual review of biomedical engineering*, vol. 1, 1999, pp. 299-329.

[23] E.A. Finol and C.H. Amon, "Flow-induced wall shear stress in abdominal aortic aneurysms: Part II--pulsatile flow hemodynamics.," *Computer methods in biomechanics and biomedical engineering*, vol. 5, 2002, pp. 319-28.

[24] L. Boussel, V. Rayz, C. McCulloch, A. Martin, G. Acevedo-Bolton, M. Lawton, R. Higashida, W.S. Smith, W.L. Young, and D. Saloner, "Aneurysm growth occurs at region of low wall shear stress: patient-specific correlation of hemodynamics and growth in a longitudinal study.," *Stroke; a journal of cerebral circulation*, vol. 39, 2008, pp. 2997-3002.

[25] H. Finlay, P. Whittaker, and P. Canham, "Collagen organization in the branching region of human brain arteries," *Stroke*, vol. 29, 1998, p. 1595.

[26] G. David and J.D. Humphrey, "Further evidence for the dynamic stability of intracranial saccular aneurysms," *Journal of Biomechanics*, vol. 36, 2003, pp. 1143-1150.

[27] M. Kroon and G.a. Holzapfel, "A theoretical model for fibroblast-controlled growth of saccular cerebral aneurysms.," *Journal of theoretical biology*, vol. 257, 2009, pp. 73-83.

[28] Y.C. Fung and S.Q. Liu, "Determination of the mechanical properties of the different layers of blood vessels in vivo.," *Proceedings of the National Academy of Sciences of the United States of America*, vol. 92, 1995, pp. 2169-73.

[29] H. Finlay, L. McCullough, and P. Canham, "Three-Dimensional Collagen Organization of Human Brain Arteries at Different Transmural Pressures," *Journal of Vascular Research*, vol. 32, 1995, pp. 301-312.

[30] P. Rissland, Y. Alemu, S. Einav, J. Ricotta, and D. Bluestein, "Abdominal aortic aneurysm risk of rupture: patient-specific FSI simulations using anisotropic model.," *Journal of biomechanical engineering*, vol. 131, 2009, p. 031001.

[31] J. SMITH, P. CANHAM, and J. STARKEY, "Orientation of collagen in the tunica adventitia of the human cerebral artery measured with polarized light and the universal stage," *Journal of Ultrastructure Research*, vol. 77, 1981, pp. 133-145.

[32] D.J. MacDonald, H.M. Finlay, and P.B. Canham, "Directional wall strength in saccular brain aneurysms from polarized light microscopy.," *Annals of biomedical engineering*, vol. 28, 2000, pp. 533-42.

[33] M. Kroon and G.a. Holzapfel, "Elastic properties of anisotropic vascular membranes examined by inverse analysis," *Computer Methods in Applied Mechanics and Engineering*, vol. 198, 2009, pp. 3622-3632.

[34] J.F. Rodríguez, C. Ruiz, M. Doblaré, and G.a. Holzapfel, "Mechanical stresses in abdominal aortic aneurysms: influence of diameter, asymmetry, and material anisotropy.," *Journal of biomechanical engineering*, vol. 130, 2008, p. 021023.

[35] P. Vena, D. Gastaldi, L. Socci, and G. Pennati, "An anisotropic model for tissue growth and remodeling during early development of cerebral aneurysms," *Computational Materials Science*, vol. 43, 2008, pp. 565-577.

[36] J.P. Vande Geest, D.E. Schmidt, M.S. Sacks, and D.a. Vorp, "The effects of anisotropy on the stress analyses of patient-specific abdominal aortic aneurysms.," *Annals of biomedical engineering*, vol. 36, 2008, pp. 921-32.

[37] P. Mitchell and J. Jakubowski, "Estimate of the maximum time interval between formation of cerebral aneurysm and rupture," *Journal of Neurology, Neurosurgery & Psychiatry*, vol. 69, 2000, pp. 760-767.

[38] R.L. Steward, C. Cheng, D.L. Wang, and P.R. LeDuc, "Probing cell structure responses through a shear and stretching mechanical stimulation technique.," *Cell biochemistry and biophysics*, vol. 56, 2010, pp. 115-24.

[39] D.a. Vorp, P.C. Lee, D.H. Wang, M.S. Makaroun, E.M. Nemoto, S. Ogawa, and M.W. Webster, "Association of intraluminal thrombus in abdominal aortic aneurysm with local hypoxia and wall weakening.," *Journal of vascular surgery : official publication, the Society for Vascular Surgery [and] International Society for Cardiovascular Surgery, North American Chapter*, vol. 34, 2001, pp. 291-9.

[40] Y. Kang, "[Experimental study on the mechanism of injury and proliferation of intima in the process of cerebral aneurysm development]," *Nippon geka hokan. Archiv für japanische Chirurgie*, vol. 59, 1990, pp. 10-26.

[41] K. Kataoka, M. Taneda, T. Asai, A. Kinoshita, M. Ito, and R. Kuroda, "Structural fragility and inflammatory response of ruptured cerebral aneurysms: a comparative study between ruptured and unruptured cerebral aneurysms," *Stroke*, vol. 30, 1999, p. 1396.

[42] D. Chyatte, G. Bruno, S. Desai, and D.R. Todor, "Inflammation and intracranial aneurysms.," *Neurosurgery*, vol. 45, 1999, pp. 1137-46; discussion 1146-7.

[43] Y.C. Fung, K. Fronek, and P. Patitucci, "Pseudoelasticity of Arteries and the Choice of its Mathematical Expression," *american journal of physiology heart and circulatory physiology*, vol. 237, 1979, pp. H620-H631.

[44] Y.C. Fung, *Biomechanics: Mechanical Properties of Living Tissues*, New York, New York, USA: Springer-Verlag New York Inc, 1993.

[45] M.L. Raghavan, J. Kratzberg, E.M. Castro de Tolosa, M.M. Hanaoka, P. Walker, and E.S. da Silva, "Regional distribution of wall thickness and failure properties of human abdominal aortic aneurysm.," *Journal of biomechanics*, vol. 39, 2006, pp. 3010-6.

[46] R.A. Ketcham and W.D. Acquisition, "optimization and interpretation of x-ray computed tomographic imagery: Applications to the geosciences," *Computers and Geosciences*, vol. 27, 2001, pp. 381-400.

[47] J.K. Park, C.S. Lee, K.B. Sim, J.S. Huh, and J.C. Park, "Imaging of the walls of saccular cerebral aneurysms with double inversion recovery black-blood sequence.," *Journal of magnetic resonance imaging : JMRI*, vol. 30, 2009, pp. 1179-83.

[48] S.C. Nicholls, J.B. Gardner, M.H. Meissner, and H.K. Johansen, "Rupture in Small Abdominal Aortic Aneurysms," *J. Vasc. Surg*, vol. 28, 1998, pp. 884-888.

[49] M.R. Elliott and a.J. Thrush, "Measurement of resolution in intravascular ultrasound images.," *Physiological measurement*, vol. 17, 1996, pp. 259-65.

[50] D. Steinman, L. Antiga, and B. Wasserman, "Overestimation of cerebral aneurysm wall thickness by black blood MRI?," *Journal of magnetic resonance imaging: JMRI*, vol. 31, 2010, p. 766.

[51] Y. Zhang, Y. Bazilevs, S. Goswami, C. Bajaj, and T. Hughes, "Patient-specific vascular NURBS modeling for isogeometric analysis of blood flow," *Computer Methods in Applied Mechanics and Engineering*, vol. 196, 2007, pp. 2943-2959.

[52] Y. Zhang, C. Bajaj, and B. Sohn, "3D finite element meshing from imaging data," *Computer methods in applied mechanics and engineering*, vol. 194, 2005, p. 50835106.

[53] R. Torii, M. Oshima, T. Kobayashi, K. Takagi, and T.E. Tezduyar, "Fluidstructure interaction modeling of blood flow and cerebral aneurysm: Significance of artery and aneurysm shapes," *Computer Methods in Applied Mechanics and Engineering*, vol. 198, 2009, pp. 3613-3621.

[54] Z. Yu, M.J. Holst, T. Hayashi, C.L. Bajaj, M.H. Ellisman, J.A. McCammon, and M. Hoshijima, "Three-dimensional geometric modeling of membrane-bound organelles in ventricular myocytes: Bridging the gap between microscopic imaging and mathematical simulation.," *Journal of structural biology*, vol. 164, 2008, pp. 304-13.

[55] Q. Sun, D. Wan, J. Liu, Y. Liu, M. Zhu, H. Hong, Y. Sun, and Q. Wang, "Influence of antegrade pulmonary blood flow on the hemodynamic performance of bidirectional cavopulmonary anastomosis: a numerical study.," *Medical engineering & physics*, vol. 31, 2009, pp. 227-33.

[56] N. Passat, C. Ronse, J. Baruthio, J. Armspach, M. Bosc, and J. Foucher, "Using multimodal MR data for segmentation and topology recovery of the cerebral superficial venous tree," *Lecture notes in computer science*, vol. 3804, 2005, p. 60.

[57] J.G. Isaksen, Y. Bazilevs, T. Kvamsdal, Y. Zhang, J.H. Kaspersen, K. Waterloo, B. Romner, and T. Ingebrigtsen, "Determination of wall tension in cerebral artery aneurysms by numerical simulation.," *Stroke; a journal of cerebral circulation*, vol. 39, 2008, pp. 3172-8.

[58] B.J. Doyle, L.G. Morris, a. Callanan, P. Kelly, D.a. Vorp, and T.M. McGloughlin, "3D reconstruction and manufacture of real abdominal aortic aneurysms: from CT scan to silicone model.," *Journal of biomechanical engineering*, vol. 130, 2008, p. 034501.

[59] B.J. Doyle, A. Callanan, and T.M. McGloughlin, "A comparison of modelling techniques for computing wall stress in abdominal aortic aneurysms.," *Biomedical engineering online*, vol. 6, 2007, p. 38.

[60] J.Y. Chueh, a.K. Wakhloo, and M.J. Gounis, "Neurovascular modeling: small-batch manufacturing of silicone vascular replicas.," *AJNR. American journal of neuroradiology*, vol. 30, 2009, pp. 1159-64.

[61] D.S. Molony, A. Callanan, E.G. Kavanagh, M.T. Walsh, and T.M. McGloughlin, "Fluid-structure interaction of a patient-specific abdominal aortic aneurysm treated with an endovascular stent-graft.," *Biomedical engineering online*, vol. 8, 2009, p. 24.

[62] N. Passat, C. Ronse, J. Baruthio, J. Armspach, and J. Foucher, "Watershed and multimodal data for brain vessel segmentation: Application to the superior sagittal sinus," *Image and Vision Computing*, vol. 25, 2007, pp. 512-521.

[63] G. Martufi, E.S. Di Martino, C.H. Amon, S.C. Muluk, and E.a. Finol, "Three-dimensional geometrical characterization of abdominal aortic aneurysms: image-based wall thickness distribution.," *Journal of biomechanical engineering*, vol. 131, 2009, p. 061015.

[64] T. McInerney and D. Terzopoulos, "Deformable models in medical image analysis: a survey.," *Medical image analysis*, vol. 1, 1996, pp. 91-108.

[65] T.D. Mabotuwana, L.K. Cheng, and A.J. Pullan, "A model of blood flow in the mesenteric arterial system.," *Biomedical engineering online*, vol. 6, 2007, p. 17.

[66] A. Valencia, F. Munoz, S. Araya, R. Rivera, and E. Bravo, "Comparison between computational fluid dynamics, fluid-structure interaction and computational structural dynamics predictions of flow-induced wall mechanics in an anatomically realistic cerebral aneurysm model," *International Journal of Computational Fluid Dynamics*, vol. 23, 2009, pp. 649-666.

[67] C. Bradley, A. Pullan, and P. Hunter, "Geometric modeling of the human torso using cubic Hermite elements," *Annals of biomedical engineering*, vol. 25, 1997, p. 96–111.

[68] G. Xu, Q. Pan, and C.L. Bajaj, "Discrete Surface Modelling Using Partial Differential Equations.," *Computer aided geometric design*, vol. 23, 2006, pp. 125-145.

[69] G. Xu, "Convergent discrete laplace-beltrami operators over triangular surfaces," *Geometric Modeling and Processing, 2004. Proceedings*, IEEE, 2004, pp. 195-204.

[70] Y. Zhang, C. Bajaj, and G. Xu, "Surface Smoothing and Quality Improvement of Quadrilateral/Hexahedral Meshes with Geometric Flow.," *Communications in numerical methods in engineering*, vol. 25, 2007, pp. 1-18.

[71] M. Meyer, M. Desbrun, P. Schröder, and A. Barr, "Discrete differential-geometry operators for triangulated 2-manifolds," *Visualization and mathematics*, vol. 3, 2002, p. 35–57.

[72] A.A. Valencia, A.M. Guzmán, E.A. Finol, and C.H. Amon, "Blood flow dynamics in saccular aneurysm models of the basilar artery.," *Journal of biomechanical engineering*, vol. 128, 2006, pp. 516-26.

[73] C.M. Scotti, J. Jimenez, S.C. Muluk, and E.a. Finol, "Wall stress and flow dynamics in abdominal aortic aneurysms: finite element analysis vs. fluid-structure interaction.," *Computer methods in biomechanics and biomedical engineering*, vol. 11, 2008, pp. 301-22.

[74] C.M. Scotti, A.D. Shkolnik, S.C. Muluk, and E.a. Finol, "Fluid-structure interaction in abdominal aortic aneurysms: effects of asymmetry and wall thickness.," *Biomedical engineering online*, vol. 4, 2005, p. 64.

[75] D.R. Hose, P.V. Lawford, A.J. Narracott, J.M. Penrose, and I.P. Jones, "Fluid-solid interaction: benchmarking of an external coupling of ansys with cfx for cardiovascular applications," *Journal of Medical Engineering & Technology*, vol. 27, 2003, pp. 23-31.

[76] C.A. Figueroa, I.E. Vignon-Clementel, K. Jansen, T.J. Hughes, and C.A. Taylor, "A coupled momentum method for modeling blood flow in three-dimensional deformable arteries," *Computer Methods in Applied Mechanics and Engineering*, 2006.

[77] O. Sahni, J. Muller, K. Jansen, M. Shephard, and C. Taylor, "Efficient anisotropic adaptive discretization of the cardiovascular system," *Computer Methods in Applied Mechanics and Engineering*, vol. 195, 2006, pp. 5634-5655.

[78] R. Torii, M. Oshima, T. Kobayashi, K. Takagi, and T.E. Tezduyar, "Fluid-structure interaction modeling of a patient-specific cerebral aneurysm: influence of structural modeling," *Comput. Mech.*, vol. 43, 2008, pp. 151-159.

[79] Y. Zhang, W. Wang, X. Liang, Y. Bazilevs, M. Hsu, T. Kvamsdal, R. Brekken, and J. Isaksen, "High-Fidelity Tetrahedral Mesh Generation from Medical Imaging Data for Fluid-Structure Interaction Analysis of Cerebral Aneurysms," *Science*, vol. 1200, 2009, pp. 1-18.

[80] J.F. Rodríguez, G. Martufi, M. Doblaré, and E.a. Finol, "The effect of material model formulation in the stress analysis of abdominal aortic aneurysms.," *Annals of biomedical engineering*, vol. 37, 2009, pp. 2218-21.

[81] J. Jensen, "An analysis of pulsed wave ultrasound systems for blood velocity estimation," *Acoustical Imaging*, 1995, pp. 377-384.

[82] Y. Bazilevs, V.M. Calo, T.J. Hughes, and Y. Zhang, "Isogeometric fluid-structure interaction: theory, algorithms, and computations," *Computational Mechanics*, vol. 43, 2008, pp. 3-37.

[83] B.J. Doyle, T.J. Corbett, A.J. Cloonan, M.R. O'Donnell, M.T. Walsh, D.a. Vorp, and T.M. McGloughlin, "Experimental modelling of aortic aneurysms: novel applications of silicone rubbers.," *Medical engineering & physics*, vol. 31, 2009, pp. 1002-12.

[84] S. Baek, R. Gleason, K. Rajagopal, and J. Humphrey, "Theory of small on large: Potential utility in computations of fluid-solid interactions in arteries," *Computer Methods in Applied Mechanics and Engineering*, vol. 196, 2007, p. 3070–3078.

[85] M. Eck, T. DeRose, T. Duchamp, H. Hoppe, M. Lounsbery, and W. Stuetzle, "Multiresolution analysis of arbitrary meshes," *Proceedings of the 22nd annual conference on Computer graphics and interactive techniques - SIGGRAPH '95*, vol. 1, 1995, pp. 173-182.

[86] M. Floater, "Parametrization and smooth approximation of surface triangulations," *Computer Aided Geometric Design*, vol. 14, 1997, p. 231250.

[87] X. Gu, S. Wang, J. Kim, Y. Zeng, Y. Wang, H. Qin, and D. Samaras, "Ricci Flow for 3D Shape Analysis," *2007 IEEE 11th International Conference on Computer Vision*, 2007, pp. 1-8.

[88] A. Sheffer, E. Praun, and K. Rose, "Mesh Parameterization Methods and Their Applications," *Foundations and Trends® in Computer Graphics and Vision*, vol. 2, 2006, pp. 105-171.

[89] P. Sander, "Sampling-efficient mesh parametrization," 2003, p. 131.

[90] X. Yin, J. Dai, S. Yau, and X. Gu, "Slit map: conformal parameterization for multiply connected surfaces," *Advances in geometric modeling and processing: 5th International Conference, GMP 2008, Hangzhou, China, April 23-25, 2008: proceedings*, Springer-Verlag New York Inc, 2008, p. 410.

[91] M. Floater, "Mean value coordinates," *Computer Aided Geometric Design*, vol. 20, 2003, pp. 19-27.

[92] M. Floater and K. Hormann, "Surface parameterization: a tutorial and survey," *Advances in multiresolution for geometric modelling*, vol. 1, 2005, pp. 1-22.

[93] B. Lévy, S. Petitjean, N. Ray, and J. Maillot, "Least squares conformal maps for automatic texture atlas generation," *ACM Transactions on Graphics*, vol. 21, 2002.

[94] K. Barner and K. Steiner, "A Displacement Driven Real-Time Deformable Model For Haptic Surgery Simulation," *14th Symposium on Haptic Interfaces for Virtual Environment and Teleoperator Systems*, 2006, pp. 499-505.

[95] T. Cui, A. Song, and J. Wu, "Simulation of a mass-spring model for global deformation," *Frontiers of Electrical and Electronic Engineering in China*, vol. 4, 2008, pp. 78-82.

[96] U. G\\"ud\\"ukbay, B. \\"Ozg\\"uç, and Y. Tokad, "A spring force formulation for elastically deformable models," *Computers \& Graphics*, vol. 21, 1997, p. 335–346.

[97] D. Terzopoulos, J. Platt, A. Barr, and K. Fleischer, "Elastically deformable models," *Proceedings of the 14th annual conference on Computer graphics and interactive techniques*, ACM New York, NY, USA, 1987, p. 205–214.

[98] X. Provot, "Deformation constraints in a mass-spring model to describe rigid cloth behaviour," *Graphics interface*, Citeseer, 1995, p. 147–147.

[99] R. Garimella and M. Shephard, "Boundary layer mesh generation for viscous flow simulations," *Int. J. Numer. Meth. Engng*, vol. 49, 2000, p. 193–218.

[100] A. Khawaja and Y. Kallinderis, "Hybrid grid generation for turbomachinery and aerospace applications," *International Journal for Numerical Methods in Engineering*, vol. 49, 2000, p. 145–166.

[101] Y. Ito, A. Shih, and B. Soni, "Reliable isotropic tetrahedral mesh generation based on an advancing front method," *13th International Meshing Roundtable*, Citeseer, 2004, p. 95–105.

[102] Y. Ito, A.M. Shih, B.K. Soni, and K. Nakahashi, "Multiple Marching Direction Approach to Generate High-Quality Hybrid Meshes," *AIAA Journal*, vol. 45, 2007, pp. 162-167.

[103] Y. Wang and S. Murgie, "Hybrid Mesh Generation for Viscous Flow Simulation," *Proceedings of the 15th International Meshing Roundtable*, Brimingham, AL: 2006, pp. 109-126.

[104] J.A. Shaw, S. Stokes, and M.A. Lucking, "The rapid and robust generation of efficient hybrid grids for rans simulations over complete aircraft," *International Journal for Numerical Methods in Fluids*, vol. 43, 2003, pp. 785-821.

[105] R. Lohner and J. Cebral, "Generation of non-isotropic unstructured grids via directional enrichment," *International Journal for Numerical Methods in Engineering*, vol. 49, 2000, pp. 219-232.

[106] S. Chalasani and D. Thompson, "Quality improvements in extruded meshes using topologically adaptive generalized elements," *International Journal for Numerical Methods in Engineering*, vol. 60, 2004, pp. 1139-1159.

[107] I. Sazonov, D. Wang, O. Hassan, K. Morgan, and N. Weatheril, "A stitching method for the generation of unstructured meshes for use with co-volume solution techniques," *Computer Methods in Applied Mechanics and Engineering*, vol. 195, 2006, pp. 1826-1845.

[108] S. Owen, "Formation of pyramid elements for hexahedra to tetrahedra transitions," *Computer Methods in Applied Mechanics and Engineering*, vol. 190, 2001, pp. 4505-4518.

[109] N. Qin and X. Liu, "Flow feature aligned grid adaptation," *International Journal for Numerical Methods in Engineering*, vol. 67, 2006, pp. 787-814.

[110] J. Krause, N. Strecker, and W. Fichtner, "Boundary-sensitive mesh generation using an offsetting technique," *International Journal for Numerical Methods in Engineering*, vol. 49, 2000, pp. 51-59.

[111] E. Johnson, Y. Zhang, and K. Shimada, "Using Parameterization and Springs to Determine Aneurysm Wall Thickness," *Proceedings of the 18th International Meshing Roundtable*, Salt Lake City, UT, USA: Springer, 2009, p. 397–414.

[112] T.D. Blacker and M.B. Stephenson, "Paving: A new approach to automated quadrilateral mesh generation," *International Journal for Numerical Methods in Engineering*, vol. 32, 1991, pp. 811-847.

[113] W.R. Quadros, K. Ramaswami, F.B. Prinz, and B. Gurumoorthy, "LayTracks: a new approach to automated geometry adaptive quadrilateral mesh generation using medial axis transform," *International Journal for Numerical Methods in Engineering*, vol. 61, 2004, pp. 209-237.

[114] Sandia National Laboratories, *CUBIT Mesh generation environment. SAND94-110*, Albuquerque, NM, USA: Sandia National Laboratories, .

[115] S. Ogoh, P.J. Fadel, R. Zhang, C. Selmer, Ø. Jans, N.H. Secher, and P.B. Raven, "Middle cerebral artery flow velocity and pulse pressure during dynamic exercise in humans.," *American journal of physiology. Heart and circulatory physiology*, vol. 288, 2005, pp. H1526-31.

[116] B. Ma, J. Lu, R.E. Harbaugh, and M.L. Raghavan, "Nonlinear anisotropic stress analysis of anatomically realistic cerebral aneurysms.," *Journal of biomechanical engineering*, vol. 129, 2007, pp. 88-96.

[117] X. Zhou, M.L. Raghavan, R.E. Harbaugh, and J. Lu, "Patient-specific wall stress analysis in cerebral aneurysms using inverse shell model.," *Annals of biomedical engineering*, vol. 38, 2010, pp. 478-89.

[118] J. Zhou and Y.C. Fung, "The degree of nonlinearity and anisotropy of blood vessel elasticity.," *Proceedings of the National Academy of Sciences of the United States of America*, vol. 94, 1997, pp. 14255-60.

[119] S.D. Williamson, Y. Lam, H.F. Younis, H. Huang, S. Patel, M.R. Kaazempur-Mofrad, and R.D. Kamm, "On the Sensitivity of Wall Stresses in Diseased Arteries to Variable Material Properties," *Journal of Biomechanical Engineering*, vol. 125, 2003, pp. 147-155.

[120] S. Petitjean, "A survey of methods for recovering quadrics in triangle meshes," *ACM Computing Surveys*, vol. 34, 2002, pp. 211-262.

[121] A. McIvor and R. Valkenburg, "A comparison of local surface geometry estimation methods," *Machine Vision and Applications*, vol. 10, 1997, p. 1726.

[122] R. Garimella and B. Swartz, "Curvature estimation for unstructured triangulations of surfaces," *Los Alamos National Laboratory*, vol. 836, 2003, pp. 0-10.

[123] J. Lu, X. Zhou, and M.L. Raghavan, "Inverse method of stress analysis for cerebral aneurysms.," *Biomechanics and modeling in mechanobiology*, vol. 7, 2008, pp. 477-86.

[124] D. Bluestein, K. Dumont, M. De Beule, J. Ricotta, P. Impellizzeri, B. Verhegghe, and P. Verdonck, "Intraluminal thrombus and risk of rupture in patient specific abdominal aortic aneurysm - FSI modelling.," *Computer methods in biomechanics and biomedical engineering*, vol. 12, 2009, pp. 73-81.

[125] M.D. Gasbarro, E.S. Di Martino, C.M. Scotti, E.a. Finol, and K. Shimada, "Computational Modeling of Abdominal Aortic Aneurysm: A New Simulation Technique that Demonstrates the Importance of Including Realistic Fluid Motion, Spinal Column, and Internal Organs," *ASME Summer Bioengineering Conference*, 2005.

[126] M.D. Gasbarro, K. Shimada, and E.S. Di Martino, "Explicit finite element method for in-vivo mechanics of abdominal aortic aneurysm," *Revue européenne de mécanique numérique*, vol. 16, 2007, pp. 337-363.